Geochronology and Geochemistry of Paleozoic to Mesozoic Granitoids in Western Inner Mongolia, China: Implications for the Tectonic Evolution of the Southern Central Asian Orogenic Belt

Qian Liu,[1] *Guochun Zhao,*[1,2,*] *Yigui Han,*[1] *Xuping Li,*[3] *Yanlin Zhu,*[1] *Paul R. Eizenhöfer,*[4] *Xiaoran Zhang,*[5] *Bo Wang,*[1] *and Regine Wingsum Tsui*[1]

1. Department of Earth Sciences, University of Hong Kong, Pokfulam Road, Hong Kong, China; 2. Department of Geology, Northwest University, Xi'an 710069, China; 3. College of Geoinformation Science and Engineering, Shandong University of Science and Technology, Qingdao 266510, China; 4. Department of Geology and Planetary Science, University of Pittsburgh, 4107 O'Hara Street, Pittsburgh, Pennsylvania 15260-3332, USA; 5. Institute of Earth Sciences, Academia Sinica, Taipei, Taiwan

ABSTRACT

Situated between the South Tianshan suture zone to the west and the Solonker suture zone to the east, the Yagan and Zhusileng-Hangwula arcs (YZHAs) in western Inner Mongolia in China occupy a critical place to investigate the tectonic history of the middle segment of the southern Central Asian Orogenic Belt (CAOB). In this work, field-based petrological studies and zircon U-Pb dating results reveal several episodes of granitic magmatism from 400 to 230 Ma in the YZHAs. Whole-rock geochemical and zircon Lu-Hf isotopic data indicate that all the 400–230 Ma granitoids underwent intensive fractional crystallization and were generated by magma mixing involving different proportions of mantle- and crust-derived materials. The ~400 Ma monzogranites show (high-K) calc-alkaline affinities, akin to S-type granitoids. They were most likely generated in a postcollisional setting, corresponding to the assembly of the YZHAs before the Early Devonian. The 298–290 Ma granitoids belong to transitional I/S-type to A-type, whereas the 280–277 Ma granitoids are typical I-type. These Permian granitoids show increasingly evolved zircon $\varepsilon_{Hf}(t)$ values and formed from crust-mantle magma mixing, suggesting an advancing subduction setting. The ~230 Ma monzogranites exhibiting fairly positive zircon $\varepsilon_{Hf}(t)$ values (+6.26 to +10.49) and high contents of mafic compositions and transition elements probably formed in a postcollisional setting after the assembly of the YZHAs and the Alxa Terrane. We infer that the final assembly of the middle segment of the southern CAOB probably occurred in the Early–Middle Permian.

Online enhancements: supplemental tables.

Introduction

The Central Asian Orogenic Belt (CAOB) is one of the largest accretionary orogens in Earth's history. It resulted from the amalgamation of the North China and Tarim Cratons to the south and the Siberian and East European Cratons to the north, through multiple episodes of accretion and collision processes in the Paleo-Asian Ocean (PAO) during Neoproterozoic to Mesozoic time (e.g., Şengör et al. 1993; Khain et al. 2003; Windley et al. 2007; Xiao et al. 2013, 2015). Early studies suggested a long-lived single-arc subduction-accretion model (e.g., Şengör et al. 1993), whereas many later studies argued for an archipelago model with multiple independent arcs in the PAO (e.g., Windley et al. 2007; Xiao et al. 2009, 2010, 2013, 2015; Wilhem et al. 2012). The late-stage evolution of the CAOB is generally considered to have occurred along its southern margin, represented by the South Tianshan suture zone to the west and the Solonker suture zone to the east. However, a consensus has not yet been reached as to the timing of the final assembly of the CAOB, because of the highly controversial suturing time of those suture zones. Some authors advocate that the suturing of the South Tianshan and Solonker suture zones occurred before

Manuscript received February 7, 2017; accepted February 20, 2018; electronically published May 16, 2018.

* Author for correspondence; email: gzhao@hku.hk.

[The Journal of Geology, 2018, volume 126, p. 451–471] 0022-1376/2018/12604-0004$15.00. DOI: 10.1086/697690

the Late Devonian to Early Carboniferous (e.g., Charvet et al. 2011; Wang et al. 2011; Xu et al. 2013), whereas some studies assert a synchronous suturing from the Late Permian to the Middle Triassic (e.g., Xiao et al. 2009, 2010, 2015). In contrast, Wilhem et al. (2012) favor a diachronous suturing, lasting from the Late Carboniferous in the west to the Permian-Triassic in the east.

Although located in a crucial junction between the South Tianshan and Solonker suture zones, the Yagan and Zhusileng-Hangwula arcs (YZHAs) in western Inner Mongolia in China (fig. 1) have received much less attention. Paleozoic to Mesozoic magmatic rocks that crop out in the YZHAs (fig. 1*B*; BGMRIM 1991; Wang et al. 1994; Wu et al. 1998; Han et al. 2010; Zheng et al. 2013) provide an ideal window to investigate the evolutionary history of the middle segment of the southern CAOB. In this contribution, we use petrological studies, zircon U-Pb dating, and whole-rock geochemical and zircon Lu-Hf isotopic analyses for a variety of Paleozoic to Mesozoic granitoids in the YZHAs to better constrain their origin and tectonic significance.

Geological Background

The YZHAs, in western Inner Mongolia, are generally considered to be the eastern extension of the

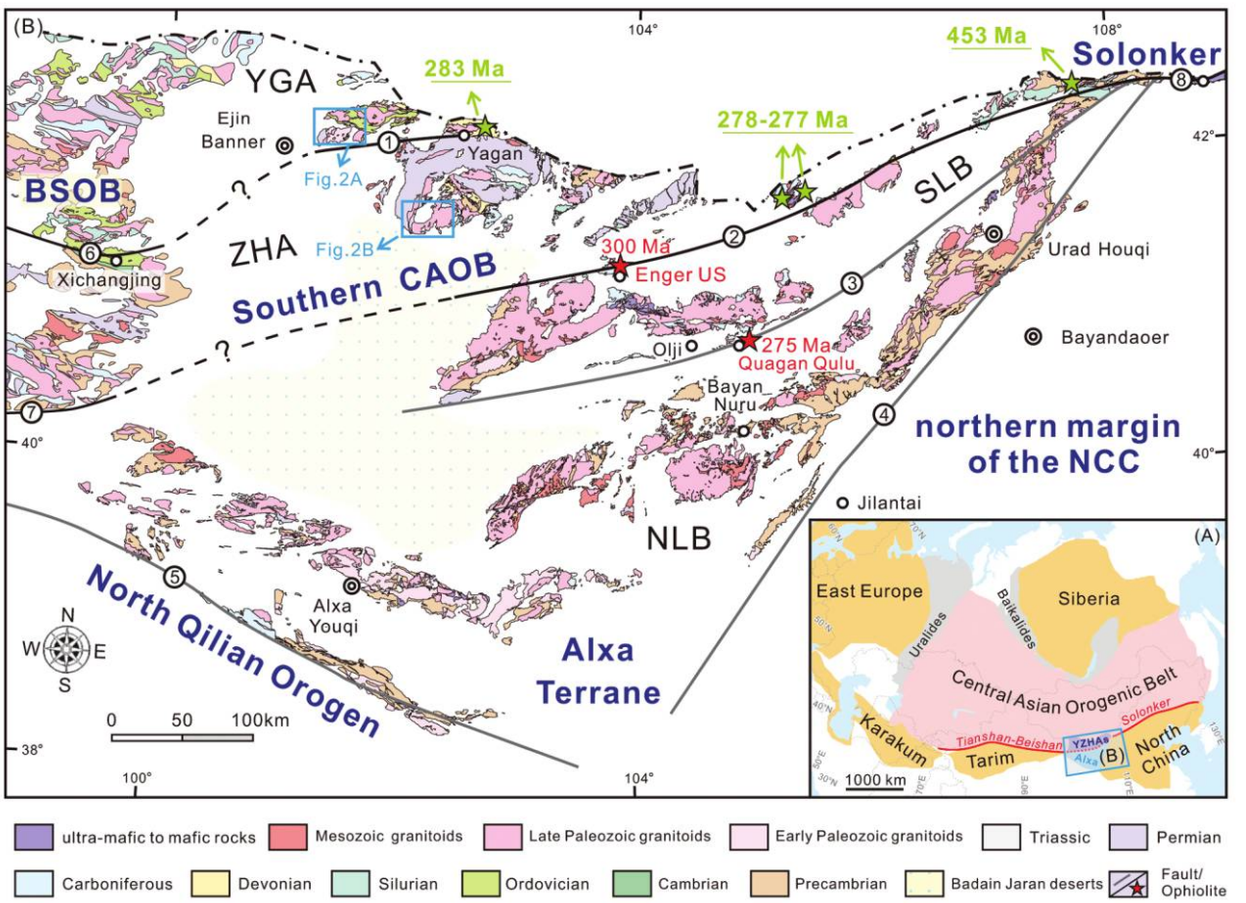

Figure 1. *A*, Simplified tectonic sketch map of China (Liu et al. 2017*b*), showing the location of the research area. YZHAs = Yagan and Zhusileng-Hangwula arcs. *B*, Geological map of the YZHAs and adjacent areas (modified after 1:200,000 geological maps from BGMRIM 1991 and geological map of Tianshan and its adjacent area; 1:1,000,000). BSOB = Beishan Orogenic Belt; CAOB = Central Asian Orogenic Belt; NCC = North China Craton; NLB = Nuru-Langshan belt; SLB = Shalazhashan belt; YGA = Yagan arc; ZHA = Zhusileng-Hangwula arc. 1 = Yagan fault; 2 = Enger Us fault; 3 = Badain Jaran fault; 4 = Langshan fault; 5 = Longshoushan fault; 6 = Hongliuhe-Niujuanzi-Xichangjing suture zone; 7 = Liuyuan suture zone; 8 = Solonker suture zone. Dating results for the granitoids in the YZHAs are from Han et al. (2010), Xu et al. (2013), and Zheng et al. (2013), and the ages of the Enger Us and Quagan Qulu ophiolitic mélanges are from Zheng et al. (2014).

Beishan Orogenic Belt (BSOB) on the basis of previous lithotectonic comparison (BGMRIM 1991; Wang et al. 1994; Wu et al. 1998). They together represent the middle segment of the southernmost CAOB and connect the South Tianshan suture zone to the west and the Solonker suture zone to the east (fig. 1*A*, 1*B*). The YZHAs connect the southern Mongolia orogenic system to the north. To the south, the YZHAs border the Alxa Terrane by the Enger Us fault, along which ~300 Ma ophiolitic mélange sporadically crops out in the Enger Us area (fig. 1*B*). This Enger Us ophiolitic mélange zone demarcates the main site of the consumption and final closure of the PAO, resulting in the assembly of the YZHAs and the Alxa Terrane (fig. 1*B*; BGMRIM 1991; Wang et al. 1994; Wu et al. 1998; Zheng et al. 2014). The Yagan fault in the YZHAs separates the Yagan arc to the north and the Zhusileng-Hangwula arc to the south (fig. 1*B*). Even though ophiolitic relics have not yet been discovered, the Yagan fault has been suggested to extend westward to the Hongliuhe-Niujuanzi-Xichangjing ophiolitic mélange zone in the BSOB, according to the comparable lithology on the south and north flanks of two boundaries (Wang et al. 1994; Wu et al. 1998).

The Yagan arc is predominantly composed of Paleozoic sedimentary sequences, with subordinate Paleozoic to Mesozoic granitoids and minor mafic intrusions and Sinian carbonates and clastic rocks (BGMRIM 1991; Wang et al. 1994; Wu et al. 1998; Zheng et al. 2013). Early Paleozoic strata are well preserved in the arc and represented by Middle Ordovician strata that consist mainly of clastic sedimentary rocks and mafic to felsic volcanic rocks, with minor cherts and limestones (BGMRIM 1991; Wu et al. 1998). The early Paleozoic volcanic rocks are predominantly basalts with transitional geochemical affinities between ocean-floor basalt and arc basalt (Wu et al. 1998), indicating that the Yagan arc was probably an immature arc in the early Paleozoic. Late Paleozoic sedimentary rocks of the Yagan arc are largely composed of clastic sedimentary rocks interbedded with voluminous felsic volcanic rocks (BGMRIM 1991; Wu et al. 1998). Because of the paucity of basalts in the late Paleozoic, a more felsic and mature arc can be inferred for the Yagan arc at that time. Accordingly, the Yagan arc was probably an immature arc in the Middle Ordovician and a mature arc in the late Paleozoic (Wu et al. 1998). In addition, Paleozoic to Mesozoic granitoids sporadically crop out in the Yagan arc, according to previous mapping (BGMRIM 1991; Wu et al. 1998; fig. 1*B*), for which accurate geochronological and geochemical data are lacking. Only a monzogranite pluton to the north of the Yagan area has yielded a zircon U-Pb age of ~283 Ma (Zheng et al. 2013). Other granitoids have not been well investigated and await further study.

In the Zhusileng-Hangwula arc, Precambrian strata are sporadically exposed (fig. 1*B*), including weakly metamorphosed carbonates and clastic rocks associated with granitic gneisses that are undated (BGMRIM 1991; Wu et al. 1998; Wang et al. 2001). Paleozoic to Mesozoic granitoids sporadically crop out in the Zhusileng-Hangwula arc, according to previous mapping (BGMRIM 1991; Wu et al. 1998), but their ages and geochemical features have not been well investigated. Only a ~453 Ma quartz diorite (Xu et al. 2013) and some 278–277 Ma granites (Han et al. 2010; Xu et al. 2013) have recently been reported in the eastern part of the arc (fig. 1*B*). However, their tectonic implications are not well understood. Paleozoic sedimentary sequences are widely distributed in the region (fig. 1*B*), in which the early Paleozoic strata are only scarcely exposed and consist of a succession of clastic rocks. Lacking volcanic rocks, these early Paleozoic sedimentary sequences have been generally regarded to have been deposited in a passive continental margin, different from the counterparts in the Yagan arc associated with voluminous volcanic rocks. In contrast, the late Paleozoic strata consist mainly of thick flysch turbidites associated with voluminous volcanic rocks, which are characteristic products on an active continental margin (BGMRIM 1991; Wu et al. 1998). Accordingly, the Zhusileng-Hangwula arc probably represented a passive continental margin in the early Paleozoic but switched to being an active continental margin in the late Paleozoic.

Sample Descriptions

In this study, 19 granitic samples were collected. Detailed sample locations, lithologies, mineral assemblages, and analytical results are summarized in table 1.

Sixteen granitic samples were collected from the western part of the Yagan arc (figs.1*B*, 2*A*). The granodiorite samples 14LQ51A and 14LQ51B and the monzogranite samples 14LQ61A and 14LQ61B intrude an early Paleozoic granitic pluton (fig. 2*A*). The former consist of quartz (~30%), alkali feldspar (~20%), plagioclase (>40%), hornblende, and biotite, with minor epidote, allanite, and apatite (fig. 3*A*). The latter comprise more quartz and alkali feldspar (fig. 3*B*). Samples 14LQ64D, 14LQ64E, 17LQ50A, 17LQ50B, 17LQ50C, and 17LQ50D are monzogranites (fig. 3*C*) that intrude the Sinian marbles and Ordovician sandstones (fig. 2*A*). The common mineral assemblages are quartz (30%–40%), varying alkali feldspar (20%–33%), plagioclase (25%–40%), and some biotite (~2%). Samples

Table 1. Summary of Sample Locations, Lithologies, Mineral Assemblages, and Analytical Results for the Paleozoic to Mesozoic Granitoids in the Yagan and Zhusileng-Hangwula Arcs

Sample	Latitude	Longitude	Lithology	Mineral assemblages	Ages (Ma)	$\varepsilon_{Hf}(t)$	T_{DM2} (Ga)
Yagan arc:							
14LQ51A	42°03′10.8″N	101°24′39.0″E	Granodiorite	Qtz 30%, Afs 17%, Pl 45%, Hbl 4%, Bt 4%, minor Ep, Aln, Ap	280	+1.53 to +3.73	1.21–1.04
14LQ51B	42°03′10.8″N	101°24′39.0″E	Granodiorite	Qtz 28%, Afs 20%, Pl 42%, Hbl 5%, Bt 5%, minor Ep, Aln, Ap			
14LQ61A	42°01′27.3″N	101°23′39.5″E	Monzogranite	Qtz 38%, Afs 35%, Pl 22%, Hbl 5%, minor Ep, Aln, Ap	277	+.41 to +3.14	1.27–1.10
14LQ61B	42°01′27.3″N	101°23′39.5″E	Monzogranite	Qtz 45%, Afs 35%, Pl 18%, Hbl 3%, minor Ep, Aln, Ap			
14LQ64D	42°01′03.2″N	101°36′38.9″E	Monzogranite	Qtz 40%, Afs 20%, Pl 38%, Bt 3%, minor Ep, Ap	397	−11.31 to +5.17	2.09–1.06
14LQ64E	42°01′03.2″N	101°36′38.9″E	Monzogranite	Qtz 40%, Afs 33%, Pl 25%, Bt 2%, minor Ep, Ap			
17LQ50A	42°01′06.5″N	101°36′37.7″E	Monzogranite	Qtz 35%, Afs 33%, Pl 30%, Bt 2%, minor Ep, Ap			
17LQ50B	42°01′06.5″N	101°36′37.7″E	Monzogranite	Qtz 35%, Afs 30%, Pl 32%, Bt 3%, minor Ep, Ap			
17LQ50C	42°01′06.5″N	101°36′37.7″E	Monzogranite	Qtz 32%, Afs 30%, Pl 35%, Bt 3%, minor Ep, Ap			
17LQ50D	42°01′06.5″N	101°36′37.7″E	Monzogranite	Qtz 30%, Afs 28%, Pl 40%, Bt 2%, minor Ep, Ap			
14LQ57A	42°09′12.3″N	101°34′56.3″E	Monzogranite	Qtz 37%, Afs 35%, Pl 25%, Bt 3%, minor Ep, Ap, Sph	230	+6.26 to +10.49	.86–.59
14LQ57B	42°09′12.3″N	101°34′56.3″E	Monzogranite	Qtz 40%, Afs 38%, Pl 25%, Bt 3%, minor Ep, Ap, Sph			
17LQ56A	42°09′12.3″N	101°34′56.3″E	Monzogranite	Qtz 40%, Afs 35%, Pl 23%, Bt 2%, minor Ep, Ap, Sph			
17LQ56B	42°09′12.3″N	101°34′56.3″E	Monzogranite	Qtz 35%, Afs 37%, Pl 25%, Bt 3%, minor Ep, Ap, Sph			
17LQ56C	42°09′12.3″N	101°34′56.3″E	Monzogranite	Qtz 35%, Afs 35%, Pl 27%, Bt 3%, minor Ep, Ap, Sph			
17LQ56D	42°09′12.3″N	101°34′56.3″E	Monzogranite	Qtz 40%, Afs 30%, Pl 25%, Bt 5%, minor Ep, Ap, Sph			
Zhusileng-Hangwula arc:							
14LQ82A	41°31′39.4″N	102°19′41.9″E	Monzogranite	Qtz 45%, Afs 32%, Pl 20%, Hbl 1%, Bt 2%, minor Ep, Aln	298	+6.84 to +9.85	.88–.69
14LQ81A	41°36′07.6″N	102°20′07.6″E	Granite	Qtz 42%, Afs 45%, Pl 10%, Bt 3%, minor Ep, Aln	290	+3.54 to +9.78	1.08–.68
14LQ81B	41°36′07.6″N	102°20′07.6″E	Granite	Qtz 45%, Afs 40%, Pl 12%, Bt 3%, minor Ep, Aln			

Note. Qtz = quartz; Afs = alkaline feldspar; Pl = plagioclase; Bt = biotite; Hbl = hornblende; Ep = epidote; Ap = apatite; Aln = allanite; Sph = sphene.

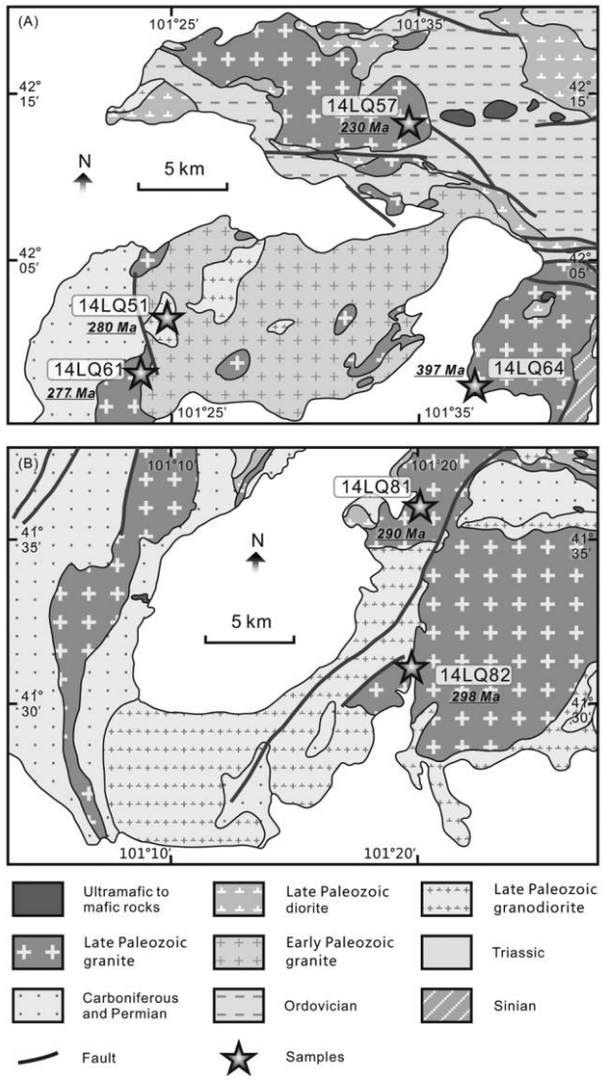

Figure 2. Geological maps showing sampling locations and ages. *A*, Ejin Banner area (modified after the 1:200,000 geological map of the Suoguodao area). *B*, Guaizihu area (after the 1:200,000 geological map of the Guaizihu area). A color version of this figure is available online.

14LQ57A, 14LQ57B, 17LQ56A, 17LQ56B, 17LQ56C, and 17LQ56D were collected from a late Paleozoic granitic pluton that intrudes the Middle Ordovician strata (fig. 2*A*). They are coarse-grained monzogranites (fig. 3*D*) with minor epidote, apatite, and titanite.

Three samples were collected from a site near the Guaizihu area in the western part of the Zhusileng-Hangwula arc (fig. 2*B*). Sample 14LQ82A is a medium- to coarse-grained monzogranite (fig. 3*E*), whereas samples 14LQ81A and 14LQ81B are fine-grained granites containing more alkali feldspar and more biotite partially altered to chlorite (fig. 3*F*).

Analytical Methods

Cathodoluminescence images for the zircons were obtained with a MonoCL3 (Gatan, Abingdon, UK) cathodoluminescence instrument attached to a scanning electron microscope (JSM-6510A, JEOL, Tokyo) at Jinyu Technology, Chongqing, China. The U-Pb zircon age for sample 14LQ64D was determined with a Geolas 193-nm laser ablation system attached to a quadrupole inductively coupled plasma mass spectrometer (LA-ICPMS) at the State Key Laboratory of Mineral Deposits Research, Nanjing University (NJU), China. A laser repetition rate of 5 Hz, energy of 10–20 J/cm^2, and a spot diameter of 32 μm were adopted for the laser system. Zircon standard GJ-1 (Jackson et al. 2004) was used for the U-Pb isotopic ratio correction. Zircon standard Mud Tank was used for quality control and yielded a mean $^{206}Pb/^{238}U$ age of 726 ± 9 Ma (n = 40), consistent, within error, with the recommended value of 732 ± 5 Ma (Black and Gulson 1978). Data reduction was performed with GLITTER 4.4 (Griffin et al. 2008), and common Pb was corrected with the method of Andersen (2002). Other samples were dated with a Photon Machines excimer 193-nm LA-ICPMS at FocuMS Technology (FMS), Nanjing, China. A laser repetition rate of 7 Hz, energy of 6.71 J/cm^2, and a spot diameter 40 μm were used. Zircon standards 91500 (Wiedenbeck et al. 1995) and GJ-1 (Jackson et al. 2004) were used for U-Pb isotopic ratio correction and as an unknown, respectively. A mean $^{206}Pb/^{238}U$ age of 601 ± 5 Ma (n = 72) was obtained for standard GJ-1, in agreement with the recommended value of 600.4 ± 0.6 Ma (Jackson et al. 2004). The raw data were processed offline with ICPMSDataCal (Liu et al. 2010). All age calculations and plotting of concordia diagrams used Isoplot (ver. 3.23; Ludwig 2003). The zircon U-Pb isotopic results are listed in table S1 (tables S1–S3 are available online).

Whole-rock major-element compositions were analyzed at NJU. Sample powder (~5 g) was first dried and mingled with 49.75% $Li_2B_4O_7$+49.75% $LiBO_2$+0.5% LiBr (~11 g). The mixture was then made into a fusion bead through partial melting and cooling at 1050°C. After that, major elements were determined by a Thermo Scientific ARL 9900 X-ray fluorescence spectrometer. The US Geological Survey rock reference materials BHVO-2 and BCR-2 were used for quality control. The uncertainties are generally less than 6% for P and 3% for other major elements.

Whole-rock trace-element concentrations were obtained with a quadrupole ICPMS at FMS after acid digestion (HF+HNO_3) of sample powder (~100 mg)

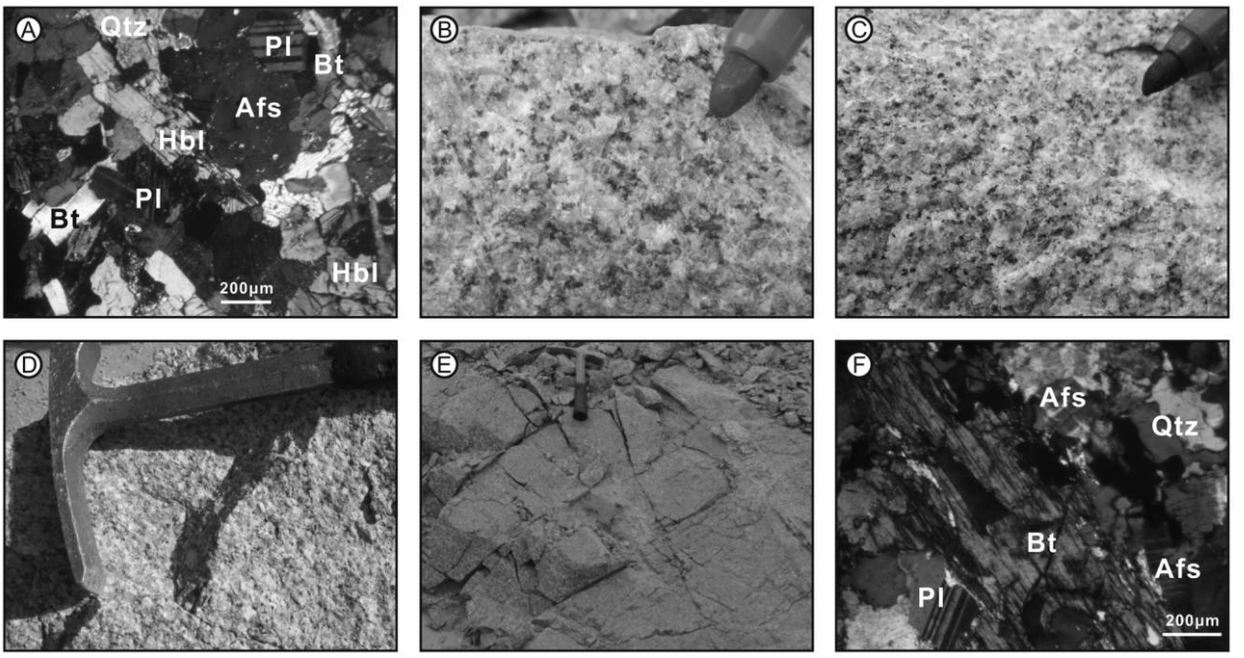

Figure 3. Representative field photographs and photomicrographs (crossed nicols). *A*, Sample 14LQ51B. *B*, Monzogranite (samples 14LQ61A and 14LQ61B) from a late Paleozoic pluton. *C*, Monzogranite (samples 14LQ64D and 14LQ64E) from a late Paleozoic pluton. *D*, Monzogranite (samples 14LQ57A and 14LQ57B) from a late Paleozoic pluton. *E*, Monzogranite (sample 14LQ82A) from a late Paleozoic pluton. *F*, Sample 14LQ81A. Afs = alkali feldspar; Bt = Biotite; Hbl = hornblende; Pl = plagioclase; Qtz = quartz. A color version of this figure is available online.

in screw-top polytetrafluoroethylene-lined stainless-steel bombs at 190°C for 12 h. For quality control, the international reference standards OU-6 of GeoPT9 (Potts et al. 2001), AMH-1 of GeoPT5 (Thompson et al. 2000), and GBPG-1 of GeoPT7 (Potts et al. 2000) were applied, indicating precision mostly better than 5%–10%. For detailed procedures, refer to Qi et al. (2000). The whole-rock elemental compositions are presented in table S2.

Zircon Lu-Hf isotopic analysis was performed with a Neptune Plasma high-resolution multicollector ICPMS equipped with a New Wave ArF 193-nm COMPex Pro laser ablation system at NJU. The working parameters were set at 44-μm ablation pit diameter, 8-Hz repetition rate, and 25-s ablation time. Two zircon standards, 91500 and Mud Tank, were analyzed to monitor the instrumental reliability and stability. The measured mean $^{176}Hf/^{177}Hf$ ratios were 0.282306 ± 0.000022 (n = 21) and 0.282502 ± 0.000017 (n = 22), respectively, in agreement with the recommended values of 0.282284 ± 0.000003 for 91500 (Wiedenbeck et al. 1995) and 0.282497 ± 0.000018 for Mud Tank (Hawkesworth and Kemp 2006). For calculation of initial $^{176}Hf/^{177}Hf$ ratios, $\varepsilon_{Hf}(t)$ values, and model ages, we used the following parameters: decay constant of ^{176}Lu: 1.865×10^{-11} per year (Scherer et al. 2001); $^{176}Hf/^{177}Hf$ and $^{176}Lu/^{177}Hf$ ratios for chondrite: 0.282772 and 0.0332 (Blichert-Toft and Albarede 1997), respectively; $^{176}Hf/^{177}Hf$ and $^{176}Lu/^{177}Hf$ ratios of depleted mantle: 0.283251 and 0.0384 (Vervoort and Blichert-Toft 1999), respectively; and $^{176}Lu/^{177}Hf$ ratio for average continental crust: 0.015 (Griffin et al. 2002). The zircon Lu-Hf isotopic data are listed in table S3.

Results

Zircon U-Pb Dating. Thirteen analyzed zircons from granodiorite sample 14LQ51A show light-brown colors and vary from prismatic to stubby forms. They exhibit oscillatory zoning (fig. 4*A*1) and have a mean Th/U ratio of 0.48, considered as autocrystic zircons forming during magma emplacement and crystallization. They yield consistent $^{206}Pb/^{238}U$ ages, with a weighted mean age of 280 ± 1 Ma (MSWD = 0.9; fig. 4*A*) interpreted as the emplacement age of the granodiorite. Two zircons yield younger ages of 254–246 Ma. They show darker and thicker zoning (fig. 4*A*2) and much higher Th and U contents (table S1), compared to those of the ~280 Ma autocrystic zircons. In this case, the zircon crystals are susceptible to radiation damage by late thermal events, resulting in Pb loss with younger apparent ages (e.g., Whitehouse et al. 1999; Geisler et al. 2003).

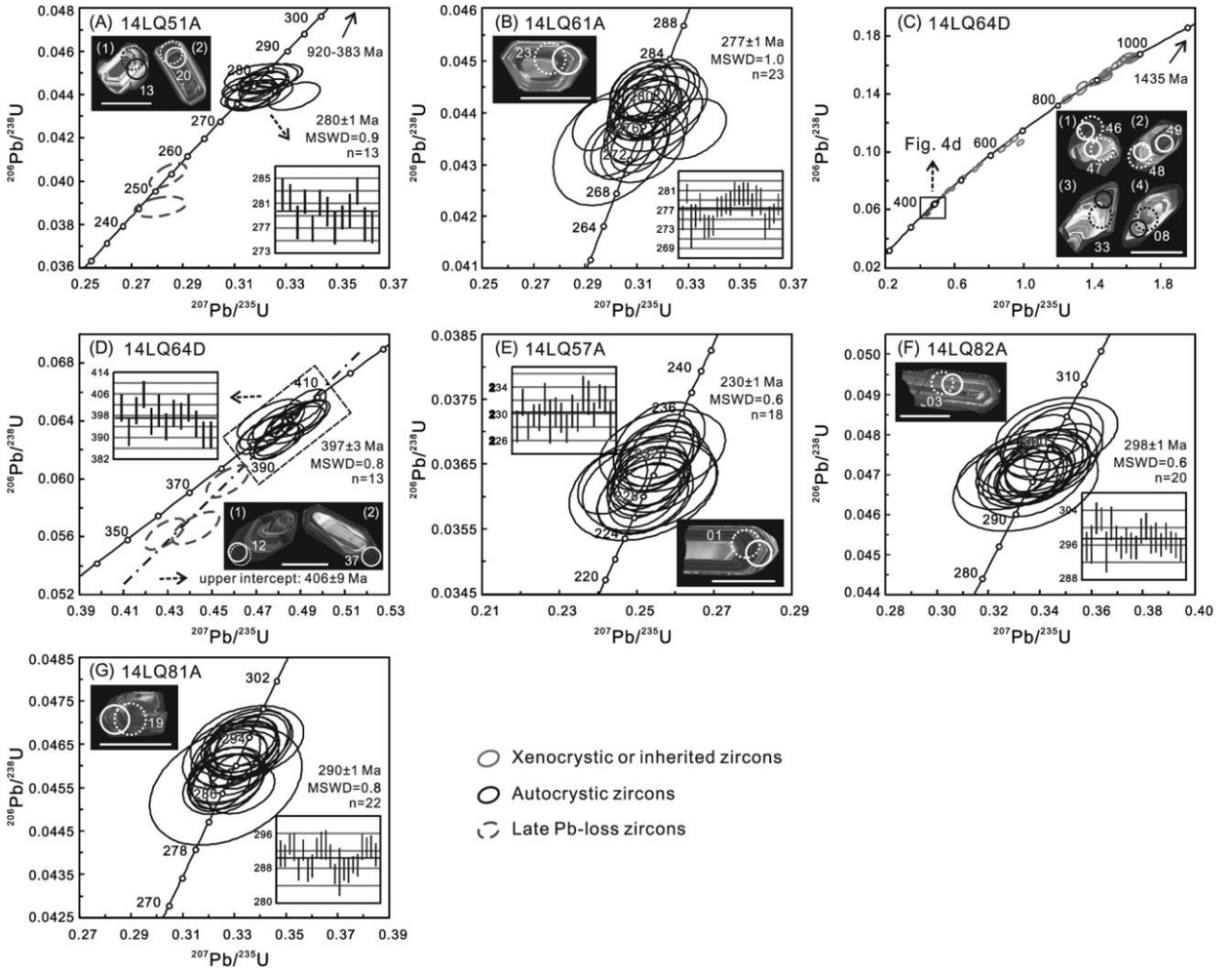

Figure 4. Representative cathodoluminescence (CL) images and U-Pb concordia diagrams of zircons from the Paleozoic to Mesozoic granitoids in the Yagan and Zhusileng-Hangwula arcs. The white scale bar is 100 μm. In CL images, the small solid and large dashed circles are locations for U-Pb dating and Hf-isotope analyses, respectively. A color version of this figure is available online.

Accordingly, the two younger zircons were possibly caused by Pb loss from the autocrystic zircons due to late events, as also evidenced by their similar Th/U ratios and Hf isotope compositions (tables S1, S3). In addition, three grains with darker colors and stubbier forms have older $^{206}Pb/^{238}U$ ages between 383 and 920 Ma, interpreted as the ages of xenocrystic or inherited zircons in the granodiorite.

The zircons from a monzogranite (sample 14LQ61A) show oscillatory zoning (fig. 4*B*) and have Th/U ratios of >0.4, reflecting a magmatic origin. Twenty-three analyses yield a weighted mean $^{206}Pb/^{238}U$ age of 277 ± 1 Ma (MSWD = 1.0; fig. 4*B*), interpreted as the emplacement age of the monzogranite.

Sample 14LQ64D is a monzogranite. The zircon cores show complex internal structures (fig. 4*C*1, 4*C*2) and yield varying ages between 1435 and 434 Ma, interpreted as the ages of inherited zircons. The autocrystic zircons in the monzogranite show oscillatory zoning for rims (fig. 4*C*1, 4*C*2) or single grains (fig. 4*C*3, 4*C*4), 13 in all, and yield a weighted mean $^{206}Pb/^{238}U$ age of 397 ± 3 Ma (MSWD = 0.8; fig. 4*D*). Similar to those from sample 14LQ51A, three zircons yielding younger apparent ages with less concordance are also obtained from sample 14LQ64D. They also show darker and thicker zoning (fig. 4*D*1, 4*D*2) and much higher Th and U contents (table S1) but similar Hf isotope compositions (table S3), compared to those of the autocrystic zircons. This suggests that their younger ages were possibly caused by Pb loss from the autocrystic zircons due to late events. In addition, coupled with the younger and autocrystic zircon ages, a discordia is produced with

an upper intercept of 406 ± 9 Ma (MSWD = 0.7; fig. 4*D*), in agreement with the weighted mean age, which further supports the nonzero Pb loss for the younger zircons. Thus, the monzogranite sample 14LQ64D is interpreted to have emplaced at ~400 Ma.

Eighteen analyzed zircons from monzogranite sample 14LQ57A display oscillatory zoning (fig. 4*E*) and high Th/U ratios, yielding a weighted mean $^{206}Pb/^{238}U$ age of 230 ± 1 Ma (MSWD = 0.6; fig. 4*E*), interpreted as the emplacement age of the monzogranite.

Zircons from monzogranite sample 14LQ82A and granite sample 14LQ81A show oscillatory zoning (fig. 4*F*, 4*G*) and Th/U ratios of >0.4, characteristic of a magmatic origin. Twenty analyses for the monzogranite and 22 for the granite yield concentrated $^{206}Pb/^{238}U$ ages with weighted means of 298 ± 1 Ma (MSWD = 0.6; fig. 4*F*) and 290 ± 1 Ma (MSWD = 0.8; fig. 4*G*), respectively. Thus, ~298 and ~290 Ma represent the respective emplacement ages of the monzogranite and the granite.

Whole-Rock Major- and Trace-Element Compositions. *Major-Element Compositions.* The Paleozoic to Mesozoic granitoids in the YZHAs show a large variation of whole-rock major-element compositions, with SiO_2 contents from 68.6% to 75.5% (table S2). They all belong to the subalkaline series (fig. 5*A*).

The ~400 Ma monzogranites in the Yagan arc exhibit high SiO_2 contents of >72% and low Al_2O_3, $Fe_2O_3^t$, Na_2O, and P_2O_5 contents (fig. 6), displaying calc-alkaline to high-K calc-alkaline (fig. 5*B*), weakly peraluminous with high A/CNK (molar ratio of $Al_2O_3/(CaO + Na_2O + K_2O)$) values of 1.06–1.09 (fig. 5*C*), and magnesian affinities (fig. 5*D*). The 298–290 Ma granitoids in the Zhusileng-Hangwula arc have fairly high SiO_2 (>74%) and Na_2O contents and low TiO_2, Al_2O_3, $Fe_2O_3^t$, MgO, and P_2O_5 contents (fig. 6). They fall into the high-K calc-alkaline and metaluminous to weakly peraluminous series (fig. 5*B*, 5*C*), and their high $FeO^t/(MgO + FeO^t)$ ratios of 0.87–0.88 indicate ferroan affinities (fig. 5*D*). Comparatively, the 280–277 Ma granitoids in the Yagan arc have a range of SiO_2 contents between 68.6% and

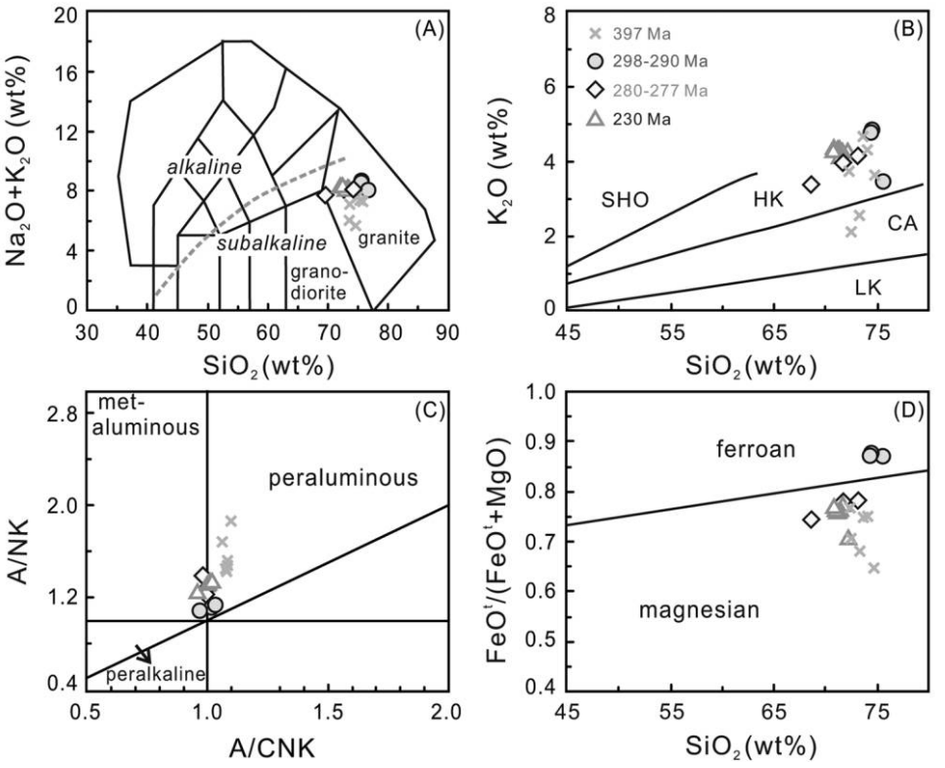

Figure 5. *A*, Total alkali versus silica (from Middlemost 1994). The dashed line is from Irvine and Baragar (1971). *B*, K_2O versus SiO_2 (Peccerillo and Taylor 1976). CA = calc-alkaline series; HK = high-K calc-alkaline series; LK = low-K tholeiite series; SHO = shoshonite series. *C*, A/CNK (molar ratio of $Al_2O_3/(CaO + Na_2O + K_2O)$) versus A/NK (molar ratio of $Al_2O_3/(Na_2O + K_2O)$) diagram (Maniar and Piccoli 1989). *D*, $FeO^t/(FeO^t + MgO)$ versus SiO_2 (after Frost et al. 2001). A color version of this figure is available online.

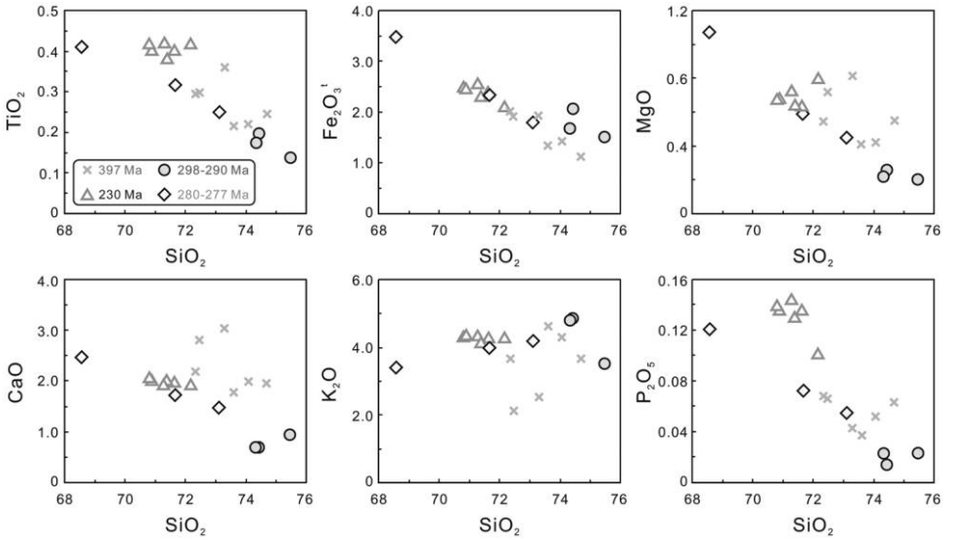

Figure 6. Harker diagrams of whole-rock major-element compositions. A color version of this figure is available online.

73.1% and belong to the high-K calc-alkaline, metaluminous, and magnesian series (fig. 5*B*–5*D*). The ~230 Ma granitoids in the Yagan arc show clustered SiO_2 contents of 70.8%–72.2% and A/CNK values of 0.96–1.02, with relatively high TiO_2, Al_2O_3, $Fe_2O_3^t$, MgO, and P_2O_5 contents (fig. 6). They are mostly akin to the high-K calc-alkaline and magnesian series (fig. 5*B*–5*D*).

Trace-Element Compositions. The ~400 Ma granitoids in the Yagan arc show relatively high Ba contents and low Y, rare earth element (REE), and high-field-strength element (HFSE, e.g., Nb, Ta, Zr, and Hf) concentrations (fig. 7). They also feature low Ga/Al (<2.3), Rb/Sr (0.34–0.99), and Rb/Ba (0.11–0.25) ratios. The 298–290 Ma granitoids in the Zhusileng-Hangwula arc have relatively low transition-element (e.g., V, Co, and Ni), Sr (26.0–55.0 ppm), and Ba contents and high concentrations of Y, REEs, and HFSEs, with high Ga/Al (3.01–4.43), Rb/Sr (2.65–6.48), and Rb/Ba (0.33–0.60) ratios. The 280–277 Ma granitoids in the Yagan arc demonstrate a large variation in trace elements (fig. 7), with low Ga/Al, Rb/Sr, and Rb/Ba ratios. The 230 Ma granitoids in the Yagan arc are characterized by higher contents of V, Co, Sr (249–268 ppm), and U (fig. 7). They exhibit low Rb/Sr and Rb/Ba ratios but high Ga/Al ratios.

The Paleozoic to Mesozoic granitoids also show different REE patterns, as shown in figure 8*A*–8*C*. The 400 Ma granitoids possess a variety of REE contents, from 93 to 166 ppm, with positive to weakly negative Eu anomalies. Their high light REE (LREE)/heavy REE (HREE; mostly >14.3) and $(La/Yb)_N$ (mostly >20.4) ratios indicate strong REE fractionation (fig. 8*A*). The 298–290 Ma granitoids display high REE contents varying from 137 to 253 ppm, markedly low REE fractionation with low LREE/HREE ratios of 4.40–5.53 and $(La/Yb)_N$ of 3.54–5.23, and strongly negative Eu anomalies with Eu/Eu^* ratios of 0.22–0.54 (fig. 8*B*). The 280–277 and 230 Ma granitoids exhibit moderate REE contents, with moderate REE fractionation (LREE/HREE ratios of 7.52–14.74) and weakly positive to negative Eu anomalies (Eu/Eu^* ratios of 0.54–1.04; fig. 8*B*, 8*C*).

As illustrated in the ocean-ridge granite–normalized incompatible-trace-element spidergram (fig. 8*D*–8*F*), almost all the granitoids demonstrate relative depletions in Nb, Sr, P, and Ti and relative enrichments in K, Rb, LREEs, and Th. Compared to the other granitoids, the 298–290 Ma (fig. 8*E*) and 230 Ma (fig. 8*F*) granitoids are relatively less depleted in Nb, Ta, and Y, with the former more depleted in Sr, P, and Ti.

Zircon Lu-Hf Isotopic Compositions. Representative dated zircons were analyzed for Lu-Hf isotopic compositions. As some younger zircons from samples 14LQ51A and 14LQ64D have been attributed to nonzero Pb loss from the earlier autocrystic zircons due to late tectonothermal events, the weighted mean ages of the autocrystic zircons, rather than the younger apparent ages, were used for isotopic calculation for the younger zircons.

The ~400 Ma zircons from sample 14LQ64D show heterogeneous Hf isotope compositions. Except for one grain with a fairly negative $\varepsilon_{Hf}(t)$ value of −11.31, the other ~400 Ma zircons exhibit a

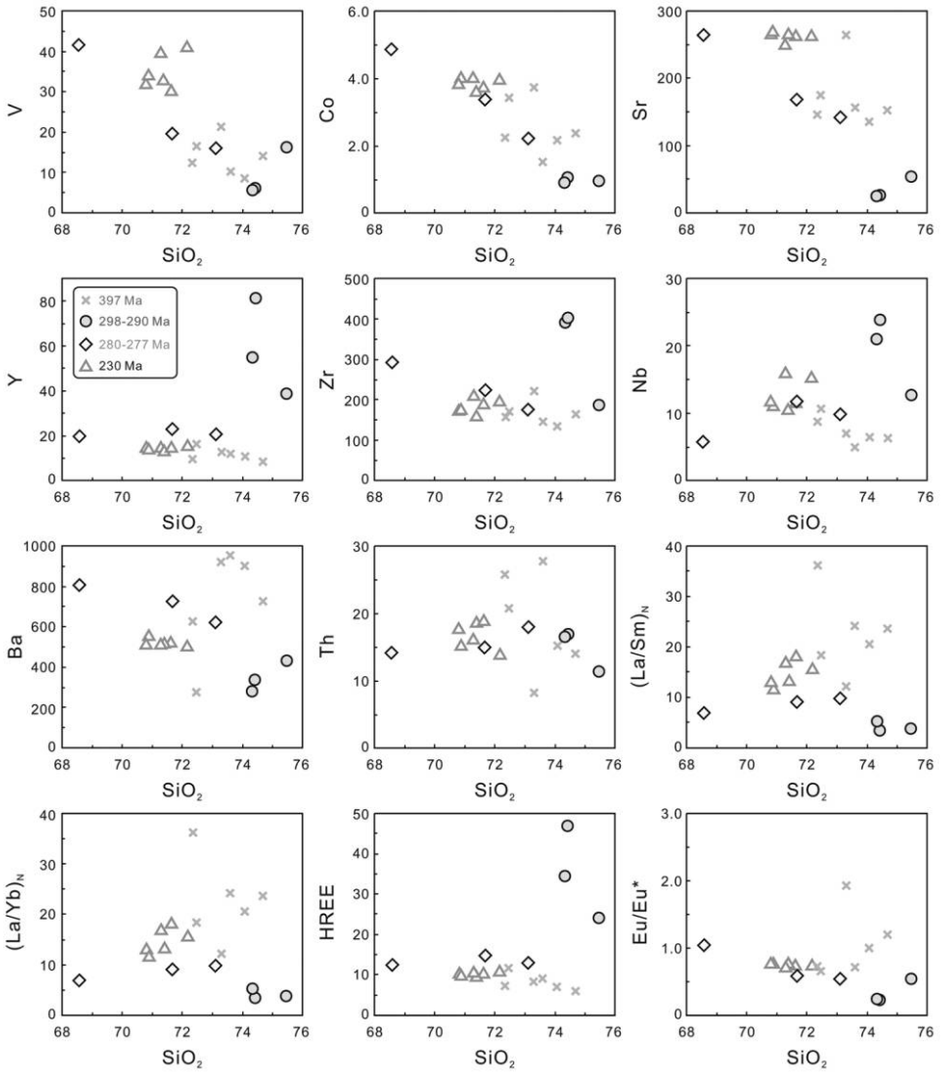

Figure 7. Harker diagrams of whole-rock trace-element compositions. A color version of this figure is available online.

large variation of $\varepsilon_{Hf}(t)$ values ranging from −3.02 to +5.17 (fig. 9), corresponding to two-stage model ages (T_{DM2}) of 1.58–1.06 Ga. In contrast, the 298–290 Ma zircons in samples 14LQ82A and 14LQ81A display more clustered and positive $\varepsilon_{Hf}(t)$ values of +3.54 to +9.85 (fig. 9) with younger T_{DM2} ages of 1.08–0.64 Ga. The 280–277 Ma grains in samples 14LQ51A and 14LQ61A show less positive $\varepsilon_{Hf}(t)$ values of +0.41 to +3.73, and therefore an increasingly enriched trend is illustrated from the 298–290 to 280–277 Ma zircons. More depleted zircon Hf isotopes are demonstrated in the ~230 Ma zircons in sample 14LQ57A showing more positive $\varepsilon_{Hf}(t)$ values of +6.26 to +10.49 and younger T_{DM2} ages of 0.86–0.59 Ga (fig. 9). In addition, the xenocrystic or inherited zircons in samples 14LQ64D and 14LQ51A exhibit complex $\varepsilon_{Hf}(t)$ values ranging from −2.27 to +5.20 (fig. 9).

Discussion

Fractional Crystallization. All the 400–230 Ma granitoids in this study show high SiO_2 contents and low CaO and mafic compositions, emphasizing a significant role of fractional crystallization before emplacement at their present level. The geochemical variations, as exhibited in the Harker diagrams (figs. 6, 7), reflect further fractional crystallization during emplacement and cooling (e.g., Yu et al. 2007). The negative correlations of TiO_2, $Fe_2O_3^t$, MgO, CaO, and P_2O_5 with respect to SiO_2 in the 400, 298–290, and 280–277 Ma granitoids (fig. 6)

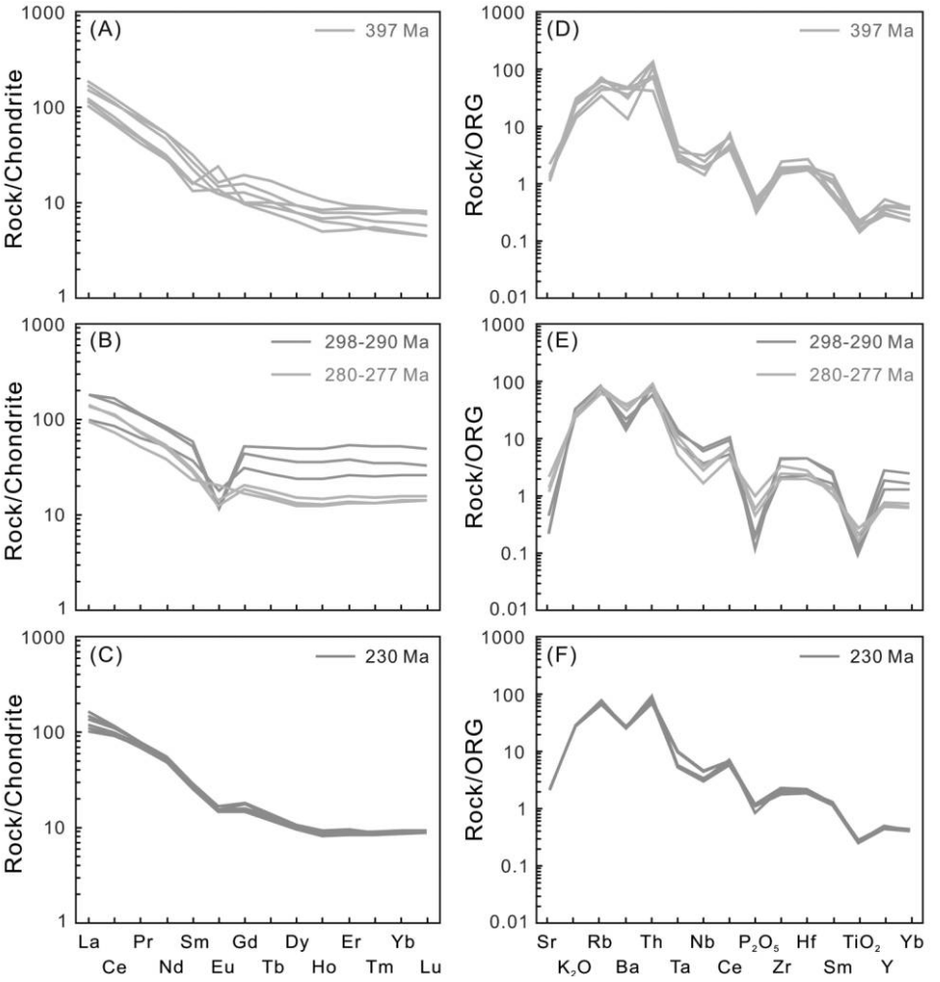

Figure 8. *A–C*, Chondrite-normalized rare earth element patterns. *D–F*, Ocean-ridge granite (ORG)–normalized incompatible-element abundances. Chondrite values are from McDonough and Sun (1995), and ORG values are from Pearce et al. (1984). A color version of this figure is available online.

indicate fractional crystallization of mafic minerals (e.g., biotite and/or hornblende) and plagioclase, with minor apatite and ilmenite. Approximately 10% fractionation of plagioclase and hornblende dominates the 400 Ma granitoids, on the basis of the fractional-crystallization modeling (fig. 10*A*), and the increasing $(La/Sm)_N$ ratios (fig. 7) suggest a greater contribution of hornblende fractionation. In addition, fractional crystallization of zircon and apatite for the 400 Ma granitoids is also highlighted by the fractional-crystallization modeling for REEs (fig. 10*B*) and the decreasing Y, Zr, Nb, and HREEs (fig. 7). Compared to the 400 Ma granitoids, the 298–290 Ma granitoids probably underwent more intensive fractional crystallization; the Sr and Ba depletions demonstrate 10%–20% fractionation of plagioclase and K-feldspar (fig. 10*A*), as also evidenced by the strongly low Sr and Ba, the markedly negative Eu anomalies, and the decreasing K and $(La/Sm)_N$ variations (figs. 6, 7). Minor fractionation of monzonite for the 298–290 Ma granitoids is also illustrated in figure 10*B*, consistent with the decreasing trend of Th (fig. 7). Comparatively, the 280–277 Ma granitoids show 10% fractionation of plagioclase (fig. 10*A*), with minor monzonite fractionation (fig. 10*B*). In addition, the 280–277 Ma granitoids display conspicuously decreasing V and Co abundances (fig. 7), which might have been attributed to fractional crystallization of biotite and ilmenite. In contrast, the fractional-crystallization processes cannot be obviously determined in the 230 Ma granitoids on the basis of their clustered geochemical compositions. Nevertheless, the decreases in Fe, P, and Th (figs. 6, 7), the negative Eu anomalies (fig. 8*C*), the decreasing La/Yb ratios with decreasing La (fig. 10*B*), and the Sr-Ba fractionation modeling

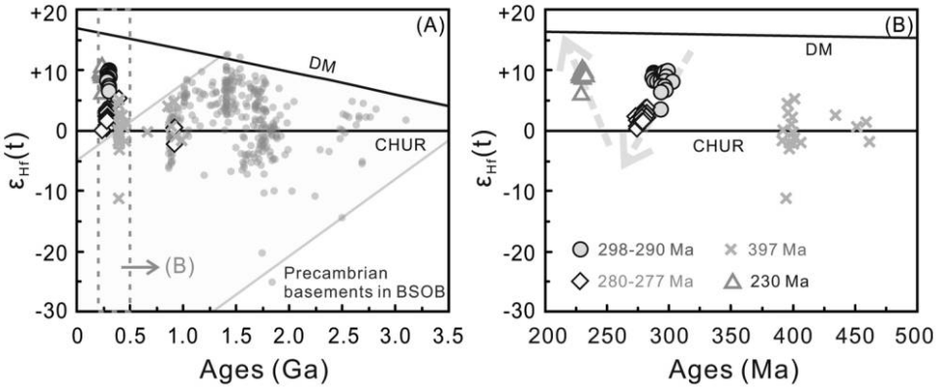

Figure 9. Zircon Lu-Hf isotopic compositions from the Paleozoic to Mesozoic granitoids in the Yagan and Zhusileng-Hangwula arcs. In *A*, the shaded area containing the dots represents the evolutionary package of zircon $\varepsilon_{Hf}(t)$ values of the Precambrian rocks in the Beishan Orogenic Belt (BSOB). The arrows in *B* outline the evolutionary trends of zircon Hf isotopes with time; the downward arrow illustrates the increasingly enriched Hf isotopes in the Early to Late Permian, whereas the upward arrow indicates a depleted trend from the Late Permian to the Triassic. CHUR = chondrite uniform reservoir; DM = depleted mantle. Data for the Meso- to Neoproterozoic basement rocks in the BSOB are from Jiang et al. (2013), Song et al. (2013), Ye et al. (2013), He et al. (2015), and Liu et al. (2015). A color version of this figure is available online.

(fig. 10*A*) suggest a major fractionation process of plagioclase, biotite, monzonite, and apatite for the 230 Ma granitoids.

Sources. The nature of source materials might have been masked by the pervasive fractional-crystallization processes in the studied granitoids (see previous section). Nonetheless, the zircon Lu-Hf isotopic compositions provide a powerful tool in deciphering the nature of source materials, because zircons can preserve the initial Hf isotopic ratios of parental magma at the time of crystallization as a result of their fairly low Lu/Hf ratios (e.g., Griffin et al. 2002, 2004; Belousova et al. 2006, 2010; Zheng et al. 2007; Kemp et al. 2008, 2009; Liu et al. 2016, 2017*a*, 2017*b*; Han et al. 2016*a*).

The ~400 Ma monzogranites have zircon T_{DM2} ages of 1.58–1.06 Ga, suggesting the involvement of Mesoproterozoic basement rocks as source materials. The Precambrian basement rocks rarely crop out in the YZHAs without any accurate age constraints. The counterparts in the adjacent BSOB contain ~1400 Ma orthogneisses, Mesoproterozoic paragneisses yielding youngest detrital zircon ages of 1530–1040 Ma, and 900–870 Ma orthogneisses and paragneisses (Jiang et al. 2013; Song et al. 2013; Ye et al. 2013; He et al. 2015; Liu et al. 2015). Their zircon Hf

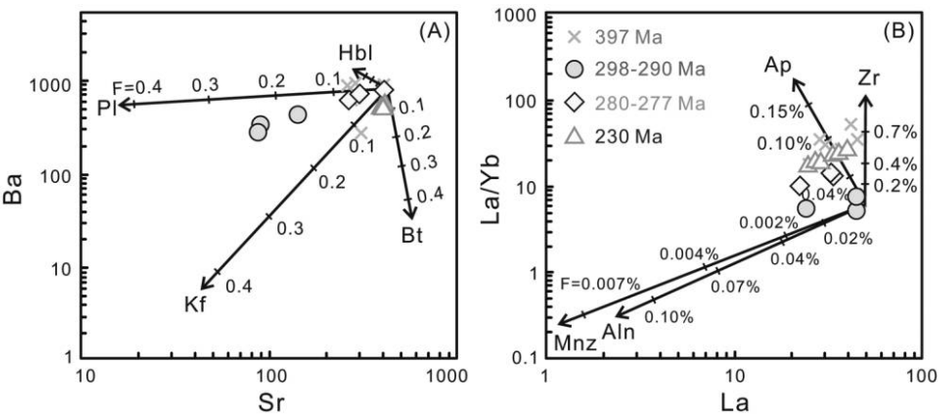

Figure 10. Fractional-crystallization modeling for the Paleozoic to Mesozoic granitoids in the Yagan and Zhusileng-Hangwula arcs. *A*, Ba-Sr variation diagram. *B*, La-La/Yb variation diagram. In the Rayleigh fractionation model, Ba, Sr, La, and Yb partitioning coefficients between minerals and granitic melt are summarized in Yu et al. (2007). *F* refers to the extent of fractionation. Aln = allanite; Ap = apatite; Bt = biotite; Hbl = hornblende; Kf = K-feldspar; Mnz = monazite; Pl = plagioclase; Zr = zircon. A color version of this figure is available online.

isotope evolutionary array covers the negative zircon $\varepsilon_{Hf}(t)$ values of the ~400 Ma monzogranites (fig. 9*A*). Therefore, the YZHAs might have also contained similar Meso- to Neoproterozoic rocks that potentially provided the ancient source materials for the ~400 Ma monzogranites. This is also in accordance with the presence of abundant Meso- to Neoproterozoic inherited zircon cores in the ~400 Ma monzogranites, which are probably derived at a deeper level from contributing source materials underlying in the region (e.g., S. A. Miller et al. 2003; J. S. Miller et al. 2007). The large range of ages for the inherited zircon cores further suggest a sedimentary source. On the other hand, the positive zircon $\varepsilon_{Hf}(t)$ values of the ~400 Ma monzogranites that lie above the package of the Precambrian rocks (fig. 9*A*) suggest the involvement of juvenile mantle-derived materials. Therefore, the parental magma of the ~400 Ma monzogranites in the YZHAs was most likely derived from mixing of sedimentary and mantle-derived materials.

All the 298–290 and 280–277 Ma granitoids in this study show positive zircon $\varepsilon_{Hf}(t)$ values lying between those of the package of the Precambrian rocks and the depleted mantle (fig. 9), suggesting crust-mantle magma-mixing processes in their petrogenesis. Magma-mixing processes in the Early Permian have also been inferred for the 283–277 Ma granitoids from the eastern part of the YZHAs, which show a large variation of whole-rock $\varepsilon_{Nd}(t)$ values, from −5.50 to +1.83 (Han et al. 2010; Zheng et al. 2013). Notably, the 298–290 Ma granitoids show zircon $\varepsilon_{Hf}(t)$ values varying from +3.54 to +9.85, which are more positive than those of the 280–277 Ma granitoids (+0.41 to +3.73). These characteristics suggest greater contribution of crust-derived materials in producing the 280–277 Ma granitic magma, in comparison with the 298–290 Ma granitic magma.

The ~230 Ma monzogranites also exhibit zircon $\varepsilon_{Hf}(t)$ values between those of the Precambrian basement rocks and the depleted mantle (fig. 9), possibly related to magma-mixing processes in the Triassic. They display zircon $\varepsilon_{Hf}(t)$ values more positive (+6.26 to +10.49) than those of the 280–277 Ma counterparts. Thus, an increasingly depleted trend for zircon Hf isotope compositions is demonstrated from the end of the Early Permian to the Triassic (fig. 9*B*), indicating a more dominant role of juvenile mantle-derived materials in the generation of the Triassic monzogranites. This inference is also evidenced by the relatively higher mafic compositions (e.g., Mg and Fe) and transition elements (e.g., V, Cr, Co, Ni, and Zn) in the ~230 Ma granitoids, compared to those of the other granitoids.

Tectonic Setting. The ~400 Ma monzogranites show transitional calc-alkaline to high-K calc-alkaline affinities and were derived from magma mixing of crust- and mantle-derived materials. Magma-mixing processes most likely occurred in a subduction or postcollisional tectonic setting (e.g., Blundy and Sparks 1992; Sylvester 1998; Tepley et al. 2000; Annen et al. 2006; Reubi and Blundy 2009). In the subduction setting, dehydration and/or partial melting of the subducted oceanic slab probably produces aqueous fluids and/or hydrous melts, by which the mantle wedge suffers metasomatism and partially melts (e.g., Martin et al. 2005; Zheng et al. 2015). The upwelling and underplating of these mantle-derived magmas result in the partial melting of crustal materials, and then the mixing of mantle- and crustal-derived magmas can produce granitoids with calc-alkaline to high-K calc-alkaline affinities, for example, the Late Permian granodiorites in East Kunlun (northern Qinghai-Tibet Plateau; Xiong et al. 2012), the Early Cretaceous magmatic complexes in southeastern China (Zhou and Li 2000), and the Late Cretaceous granitoids in northeastern Turkey (Karsli et al. 2010). Alternatively, in the postcollisional setting, delamination of substantial amounts of mantle lithosphere is prone to take place after syncollisional crustal thickening. Upwelling asthenosphere could rise to shallow-mantle depths and produce mafic magmas that provide heat and materials to the crust (e.g., Sylvester 1998). The mantle- and crust-derived magma can potentially mix in this scenario, as exemplified by the granitoids in the Lachlan Fold Belt of southeastern Australia and the Caledonian orogeny of Britain (Pitcher 1983; Sylvester 1998).

For three reasons, a postcollisional setting is preferred. (1) The regional unconformity between the Late Silurian and Early Devonian sedimentary sequences in the YZHAs (BGMRIM 1991) is supportive of the Early Devonian connection of the Yagan arc and the Zhusileng-Hangwula arc. (2) The ~400 Ma monzogranites are more akin to S-type granitoids, as indicated by their high A/CNK ratios (1.06–1.09) and the absence of hornblende. This explanation is also consistent with the large range of ages for the inherited zircon cores in the ~400 Ma monzogranites, suggesting a major contribution of sedimentary source materials (e.g., Chappell and White 1974, 1992, 2001; Patiño Douce 1999). S-type granitoids more likely form in a postcollisional setting after the connection of two tectonic units (e.g., Pearce 1996; Sylvester 1998). (3) Despite the paucity of ophiolitic relics along the Yagan fault, previous studies proposed that the Yagan fault extends westward to the Hongliuhe-Niujuanzi-Xichangjing ophiolitic mélange zone in the BSOB (BGMRIM 1991; Wu et al. 1998). This inference was based on the comparison of lithologic units on the south and north flanks of

the ophiolitic mélange zone (Wang et al. 1994; Wu et al. 1998). The youngest ophiolitic relics are represented by ~410 Ma gabbros in the nearby Niujuanzi area (Tian et al. 2013) and ~426 Ma gabbros in the Hongliuhe area. Some massive granitic plutons intrude the gabbros in the ophiolitic relics, and thus the crystallization ages of these granitic plutons (412–405 Ma; Guo et al. 2006; Yu et al. 2006; Zhang and Guo 2008) provide an upper limit for the formation age of the ophiolitic relics. Accordingly, two tectonic units on both flanks of the Hongliuhe-Niujuanzi-Xichangjing ophiolitic mélange zone in the BSOB might have welded at the beginning of the Early Devonian (Xiao et al. 2010). As a consequence, the Yagan arc might have also connected with the Zhusileng-Hangwula arc in the earliest Devonian. Therefore, the ~400 Ma monzogranites in the YZHAs most likely formed in a postcollisional setting.

The 298–290 Ma granitoids show high HFSE (e.g., Nb, Ta, Zr, and Hf) contents and high Ga/Al, Rb/Sr and Rb/Ba ratios, akin to transitional granitoids between high felsic I/S-type and A-type, whereas the 280–277 Ma granitoids with metaluminous and magnesian affinities are typical I-type (e.g., Whalen et al. 1987; Eby 1990; Frost et al. 2001). These rock associations derived from magma mixing are prone to occur in a subduction or postcollisional tectonic setting (e.g., Blundy and Sparks 1992; Sylvester 1998; Tepley et al. 2000; Yu et al. 2005; Annen et al. 2006; Reubi and Blundy 2009; Liu et al. 2015, 2016, 2017*b*). We favor a subduction tectonic setting for the following reasons. (1) The Permian zircons in the 298–290 and 280–277 Ma granitoids show increasingly enriched Hf isotope compositions (fig. 9*B*), which might have been associated with an advancing subduction setting. The advancing subduction develops where the rate of overall plate convergence is greater than the rate of subduction, resulting in topographically high mountains, antithetic thrust belts, and intensive erosion and denudation (e.g., Royden and Burchfiel 1989). In this scenario, more crustal materials are involved during magma generation with time, which contradicts an extensional postcollisional setting involving more mafic materials (e.g., Miller et al. 2003; Kemp et al. 2009; Collins et al. 2011; Roberts et al. 2013; Zheng et al. 2015; Han et al. 2016*a*; Liu et al. 2016, 2017*a*, 2017*b*). (2) The assembly of the YZHAs and the Alxa Terrane due to the final closure of the PAO was considered to occur at 280–265 Ma (Liu et al. 2017*a*, 2017*b*), and thus the YZHAs might have not been subject to a postcollisional regime before the Middle Permian. (3) The Early Permian subduction processes also took place in the adjacent BSOB. The Liuyuan ophiolitic mélange zone was interpreted to represent the site of the final closure of the PAO in the BSOB, as evidenced by ~286 Ma mafic rocks with suprasubduction-zone affinities (Xiao et al. 2010; Mao et al. 2012).

The ~230 Ma monzogranites probably formed in a subsequent postcollisional setting after the assembly of the YZHAs and the Alxa Terrane. Their high contents of mafic compositions (e.g., Mg and Fe) and transition elements (e.g., V, Cr, Co, Ni, and Zn) and fairly positive zircon $\varepsilon_{Hf}(t)$ values are also consistent with the postcollisional setting where the asthenospheric mantle was involved to produce magmas with more juvenile isotopic compositions (e.g. Smits et al. 2014; Han et al. 2016*a*; Liu et al. 2017*a*, 2017*b*). This explanation is also consistent with the magmatic and structural records in the adjacent areas. For examples, the ~228 Ma granitoids showing potassic and shoshonitic affinities and synemplacement extensional deformation have also been reported in Onch Hayrhan, to the east of Yagan in the southernmost Sino-Mongolian border in China, favoring a postcollisional extensional environment (Wang et al. 2004). In addition, voluminous 240–217 Ma high-felsic I-type and A-type granitoids with minor 250–220 Ma ultramafic to mafic rocks in the BSOB, as well as 255–239 Ma ultramafic to felsic plutonic rocks in the Alxa Terrane, were all considered products of a postcollisional regime (C. Liu et al. 2006; S. H. Zhang et al. 2010; Y. Y. Zhang et al. 2011; Li et al. 2012; Tian et al. 2013; Shi et al. 2014*a*, 2014*b*; Wang et al. 2015; Q. Liu et al. 2017*a*). Furthermore, the Middle Triassic north-south refolding of the Upper Permian volcanosedimentary successions in the BSOB (e.g., Tian et al. 2013; Wang et al. 2017) has been considered to correspond to a local rift system in the BSOB in the Middle Triassic (e.g., Wang et al. 2017), which is also consistent with our argument for an extensional setting. Collectively, the ~230 Ma monzogranites in the YZHAs most likely formed in a postcollisional regime.

Magmatic Episodes in the YZHAs. Zircon U-Pb dating results from this work and previous studies indicate several magmatic episodes in the YZHAs between 453 and 230 Ma (Wang et al. 2001; Han et al. 2010; Xu et al. 2013; Zheng et al. 2013; this study). These include a major episode during Early Permian (298–277 Ma) time and minor episodes during Late Ordovician (~453 Ma), Late Devonian (~400 Ma), and Late Triassic (~230 Ma) time.

The early Paleozoic magmatism has been rarely reported in the YZHAs, with one ~453 Ma arc-related dioritic pluton recognized in the easternmost part (Xu et al. 2013). In contrast, our new results reveal a variety of middle to late Paleozoic granitoids in the western part of the YZHAs, with emplacement ages between 400 and 277 Ma. The ~400 Ma monzo-

granites show calc-alkaline to high-K calc-alkaline affinities, more akin to S-type granitoids. The Early Permian granitic magmatism is represented by the 298–280 Ma transitional I/S-type to A-type granites and monzogranites, as well as the 280–277 Ma I-type monzogranites and granodiorites. Besides, several 283–277 Ma felsic I/S-type granitoids have also been reported in the western and middle parts of the YZHAs (fig. 1*B*; Han et al. 2010; Zheng et al. 2013). In addition, a ~230 Ma monzogranite pluton in the western part of the YZHAs is discovered in this study (fig. 2*A*).

Tectonic Evolution of the YZHAs. Considered as the eastern extension of the BSOB (BGMRIM 1991; Wang et al. 1994; Wu et al. 1998), the YZHAs might also have Meso- to Neoproterozoic basement rocks; this is different from the Alxa Terrane and the Tarim and North China Cratons, which mainly consist of Neoarchean to Mesoproterozoic basements (e.g., Zhao et al. 2001, 2005; Long et al. 2010, 2011; Gong et al. 2012; Ge et al. 2013*a*, 2013*b*, 2014; Zhang et al. 2013). This inference is also in accordance with the coeval inherited zircons in the studied granitoids (samples 14LQ51A and 14LQ64D). The postulated basement rocks might have played an important role in providing old crustal materials for the formation of the Paleozoic to Mesozoic magmatic rocks in the YZHAs. The lack of outcrops of these basement rocks possibly results from the large coverage of both desert and the Phanerozoic magmatic and sedimentary rocks in the region.

In the early Paleozoic, the Zhusileng-Hangwula arc was probably a passive continental margin (BGMRIM 1991; Wu et al. 1998), whereas the Yagan arc was an immature arc since the Middle Ordovician (BGMRIM 1991; Wu et al. 1998). The YZHAs have generally been considered the continuation of the southern Mongolia orogenic system, as a result of the southward accretion along the southern active margin of the Siberia Craton since the Neoproterozoic to the Paleozoic-Mesozoic due to the northward subduction of the PAO (e.g., Şengör et al. 1993; Khain et al. 2003; Windley et al. 2007; Xiao et al. 2009, 2013, 2015). Accordingly, the voluminous Middle Ordovician basalts in the Yagan arc were probably related to the northward subduction of the ocean intervening between the Yagan arc and the Zhusileng-Hangwula arc (fig. 11*A*). This inference is also consistent with the coeval northward subduction process in the BSOB established by Xiao et al. (2010). The final closure of this oceanic lithosphere, leading to the assembly of these two arcs, possibly occurred before the Early Devonian (fig. 11*B*), followed by a subsequent postcollisional setting giving birth to the ~400 Ma monzogranites in the region.

During Early Permian time, the combined YZHAs were subject to a subduction setting, associated with the further northern subduction of the PAO (fig. 11*C*). On the other hand, the Alxa Terrane also contains coeval arc-related magmatic rocks, which have been interpreted to correspond to the southward subduction of the PAO (Liu et al. 2017*a*, 2017*b*). Therefore, divergent double-sided subduction of the PAO lithosphere between the YZHAs and the Alxa Terrane took place (fig. 11*C*). Dehydration of the oceanic lithosphere induced the partial melting of the mantle wedge to produce mafic magmas. The upwelling and underplating of these mantle-derived magmas resulted in the partial melting of the Precambrian basement rocks, and then the mixing of mantle- and crust-derived magmas produced a variety of 298–277 Ma granitoids in the region. The compression in the overriding YZHAs as a consequence of advancing subduction processes caused a local crustal thickening and intense subduction erosion, leading to large involvements of ancient crustal materials in generating granitic magmas with increasingly evolved zircon Hf and whole-rock Nd isotope signatures.

In the Late Triassic, the YZHAs experienced extension and crustal thinning in a postcollisional regime posterior to the disappearance of the PAO (fig. 11*D*). In this scenario, the PAO lithosphere might have not been tied to either overlying unit but might have detached and sunk into the mantle as a result of density contrast (e.g., Soesoo et al. 1997). Inflow of mantle materials and melts filled the gap above the sinking oceanic slab, resulting in thermal perturbation and partial melting of asthenosphere, lithospheric mantle wedge, and ancient crust (e.g., Soesoo et al. 1997). The asthenosphere-derived magma might have partially mixed with the crust-derived magma and given rise to the ~230 Ma granitoids in the YZHAs with more juvenile isotopic records.

Notably, the period from the Permian to the Triassic represents the late-stage evolution of the middle segment of the southern CAOB. The youngest arc-related granitoids in the YZHAs yield an emplacement age of ~277 Ma, whereas the oldest postcollisional granitoids formed at ~230 Ma. Accordingly, the final closure of the PAO between the YZHAs and the Alxa Terrane probably occurred at 277–230 Ma. This inference is in accordance with the integrated magmatic, structural, and sedimentary study in the Alxa Terrane (Liu et al. 2017*a*, 2017*b*), which suggests ca. 280–265 Ma for the closure time of the PAO between the YZHAs and the Alxa Terrane. Therefore, the final assembly of the YZHAs and the Alxa Terrane in the middle segment of the southern CAOB probably took place in the Early–Middle Permian. On the basis of previous constraints on the

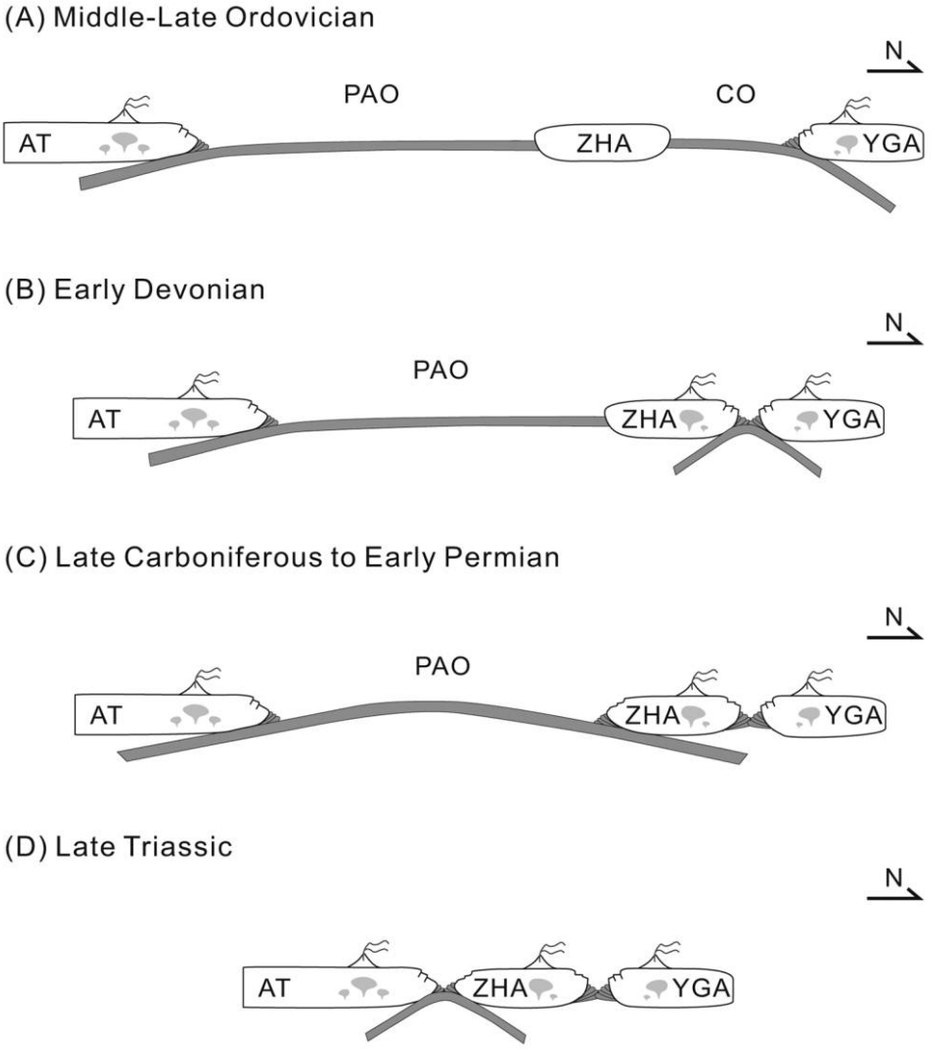

Figure 11. Tentative tectonic scenario showing the Paleozoic evolution of the Yagan and Zhusileng-Hangwula arcs and the Alxa Terrene. AT = Alxa Terrane; CO = ocean between the YGA and the ZHA; PAO = Paleo-Asian Ocean; YGA = Yagan arc; ZHA = Zhusileng-Hangwula arc.

timing of the final assembly of the western and eastern segments of the southern CAOB (e.g., Gao et al. 2011; B. F. Han et al. 2011; Y. G. Han et al. 2016*b*; Klemd et al. 2011; Eizenhöfer et al. 2014, 2015*a*, 2015*b*; Zhang et al. 2015*a*, 2015*b*, 2016; Liu et al. 2017*a*, 2017*b*), a diachronous assembly of the southern CAOB is inferred, starting in the west along the northern margin of the Tarim Craton at ca. 320–300 Ma, in the BSOB and the Alxa Terrane at ca. 280–265 Ma, and progressing to the east along the northern margin of the North China Craton at ca. 260–245 Ma.

Conclusions

1. LA-ICPMS zircon U-Pb dating results in this study reveal several episodes of granitic magmatism in the YZHAs, including the ~400 Ma monzogranites, the 298–290 Ma monzogranites and granites, the 280–277 Ma granodiorites and monzogranites, and the ~230 Ma monzogranites.

2. Whole-rock geochemical and zircon Lu-Hf isotopic compositions indicate that the 400–230 Ma granitoids underwent pervasive fractional crystallization and were generated by magma mixing involving different proportions of mantle- and crust-derived materials.

3. The 298–277 Ma granitoids are considered to have formed in a subduction setting, whereas the ~400 and ~230 Ma monzogranites were most likely generated in a postcollisional setting.

4. Since the Middle Ordovician, the Zhusileng-Hangwula arc was a passive continental margin,

while the Yagan arc was subject to the northward subduction of the PAO. The two arcs converged before the Early Devonian. An advancing subduction of the PAO beneath the YZHAs took place during Early Permian time. The final closure of the middle segment of the PAO, resulting in the assembly of the YZHAs and the Alxa Terrane, probably occurred in the Early–Middle Permian.

ACKNOWLEDGMENTS

This work was financially supported by the National Natural Science Foundation of China (NSFC) Project (41190075) titled "Final Closure of the Paleo-Asian Ocean and Reconstruction of East Asian Blocks in Pangea," the fifth research project in the NSFC Major Program (41190070) "Reconstruction of East Asian Blocks in Pangea"; the Hong Kong Research Grants Council General Research Fund (HKU7063/13P and 17301915); NSFC General Projects (41230207 and 41390441); and University of Hong Kong Seed Funding Programmes for Basic Research (201311159126 and 201611159210). We sincerely thank L. Wu, B. Wu, J. Gao, L. Li, G. Zeng, and T. Yang for their assistance in experimental analyses.

REFERENCES CITED

Andersen, T. 2002. Correction of common Pb in U-Pb analyses that do not report ^{204}Pb. Chem. Geol. 192:59–79.

Annen, C.; Blundy, J. D.; and Sparks, R. S. J. 2006. The genesis of intermediate and silicic magmas in deep crustal hot zones. J. Petrol. 47:505–539.

Belousova, E. A.; Griffin, W. L.; and O'Reilly, S. Y. 2006. Zircon crystal morphology, trace element signatures and Hf isotope composition as a tool for petrogenetic modelling: examples from Eastern Australian granitoids. J. Petrol. 47:329–353.

Belousova, E. A.; Kostitsyn, Y. A.; Griffin, W. L.; Begg, G. C.; O'Reilly, S. Y.; and Pearson, N. J. 2010. The growth of the continental crust: constraints from zircon Hf-isotope data. Lithos 119:457–466.

BGMRIM (Bureau of Geology and Mineral Resources of Inner Mongolia Autonomous Region). 1991. Regional geology of Inner Mongol Autonomous Region. Beijing, Geological Publishing House, 725 p. (in Chinese).

Black, L. P., and Gulson, B. L. 1978. The age of the Mud Tank carbonatite, Strangways Range, Northern Territory. BMR J. Aust. Geol. Geophys. 3:227–232.

Blichert-Toft, J., and Albarede, F. 1997. The Lu-Hf isotope geochemistry of chondrites and the evolution of the mantle-crust system. Earth Planet. Sci. Lett. 148:243–258.

Blundy, J. D., and Sparks, R. S. J. 1992. Petrogenesis of mafic inclusions in granitoids of the Adamello Massif, Italy. J. Petrol. 33:1039–1104.

Chappell, B. W., and White, A. J. R. 1974. Two contrasting granites types. Pac. Geol. 8:173–174.

———. 1992. I- and S-type granites in the Lachlan Fold Belt. Trans. R. Soc. Edinb. Earth Sci. 83:1–26.

———. 2001. Two contrasting granites types: 25 years later. Aust. J. Earth Sci. 48:489–499.

Charvet, J.; Shu, L. S.; Laurent-Charvet, S.; Wang, B.; Faure, M.; Cluzel, D.; Chen, Y.; and De Jong, K. 2011. Palaeozoic tectonic evolution of the Tianshan belt, NW China. Sci. China Ser. D Earth Sci. 54:166–184.

Collins, W. J.; Belousova, E. A.; Kemp, A. I. S.; and Murphy, J. B. 2011. Two contrasting Phanerozoic orogenic systems revealed by hafnium isotope data. Nat. Geosci. 4:333–337.

Eby, G. N. 1990. The A-type granitoids: a review of their occurrence and chemical characteristics and speculations on their petrogenesis. Lithos 26:115–134.

Eizenhöfer, P. R.; Zhao, G. C.; Sun, M.; Zhang, J.; Han, Y. G.; and Hou, W. Z. 2015*a*. Geochronological and Hf isotopic variability of detrital zircons in Paleozoic strata across the accretionary collision zone between the North China craton and Mongolian arcs and tectonic implications. Geol. Soc. Am. Bull. 127:1422–1436.

Eizenhöfer, P. R.; Zhao, G. C.; Zhang, J.; Han, Y. G.; Hou, W. Z.; Liu, D. X.; and Wang, B. 2015*b*. Geochemical characteristics of the Permian basins and their provenances across the Solonker Suture Zone: assessment of net crustal growth during the closure of the Palaeo-Asian Ocean. Lithos 224–225:240–255.

Eizenhöfer, P. R.; Zhao, G. C.; Zhang, J.; and Sun, M. 2014. Final closure of the Paleo-Asian Ocean along the Solonker Suture Zone: constraints from geochronological and geochemical data of Permian volcanic and sedimentary rocks. Tectonics 33:441–463.

Frost, B. R.; Barnes, C. G.; Collins, W. J.; Arculus, R. J.; Ellis, D. J.; and Frost, C. D. 2001. A geochemical classification for granitic rocks. J. Petrol. 42:2033–2048.

Gao, J.; Klemd, R.; Qian, Q.; Zhang, X.; Li, J. L.; Jiang, T.; and Yang, Y. Q. 2011. The collision between the Yili and Tarim blocks of the southwestern Altaids: geochemical and age constraints of a leucogranite dike crosscutting the HP-LT metamorphic belt in the Chinese Tianshan Orogen. Tectonophysics 499:118–131.

Ge, R. F.; Zhu, W. B.; Wilde, S. A.; and He, J. W. 2014. Zircon U-Pb-Lu-Hf-O isotopic evidence for ≥3.5 Ga crustal growth, reworking and differentiation in the northern Tarim Craton. Precambrian Res. 249:115–128.

Ge, R. F.; Zhu, W. B.; Wu, H. L.; He, J. W.; and Zheng, B. H. 2013*a*. Zircon U-Pb ages and Lu-Hf isotopes of Paleoproterozoic metasedimentary rocks in the Korla Complex, NW China: implications for metamorphic zircon formation and geological evolution of the Tarim Craton. Precambrian Res. 231:1–18.

Ge, R. F.; Zhu, W. B.; Wu, H. L.; Zheng, B. H.; and He, J. W. 2013*b*. Timing and mechanisms of multiple episodes of migmatization in the Korla Complex, northern Tarim Craton, NW China: constraints from zircon U-Pb-Lu-Hf isotopes and implications for crustal growth. Precambrian Res. 231:136–156.

Geisler, T.; Rashwan, A. A.; Rahn, M. K. W.; Poller, U.; Zwingmann, H.; Pidgeon, R. T.; Schleicher, H.; and Tomaschek, F. 2003. Low-temperature hydrothermal alteration of natural metamict zircons from the Eastern Desert, Egypt. Mineral. Mag. 67(3):485–508.

Gong, J. H.; Zhang, J. X.; Yu, S. Y.; Li, H. K.; and Hou, K. J. 2012. Ca. 2.5 Ga TTG rocks in the western Alxa Block and their implications. Chin. Sci. Bull. 57:4064–4076.

Griffin, W. L.; Belousova, E. A.; Shee, S. R.; Pearson, N. J.; and O'Reilly, S. Y. 2004. Archean crustal evolution in the northern Yilgarn Craton: U-Pb and Hf-isotope evidence from detrital zircons. Precambrian Res. 131:231–282.

Griffin, W. L.; Powell, W. J.; Pearson, N. J.; and O'Reilly, S. Y. 2008. GLITTER: data reduction software for laser ablation ICP-MS. *In* Sylvester, P., ed. Laser ablation-ICP-MS in the earth sciences: current practices and outstanding issues. Short Course Ser. no. 40. Québec, Mineralogical Association of Canada, p. 308–311.

Griffin, W. L.; Wang, X.; Jackson, S. E.; Pearson, N. J.; and O'Reilly, S. Y. 2002. Zircon geochemistry and magma mixing, SE China: in-situ analysis of Hf isotopes, Tonglu and Pingtan igneous complexes. Lithos 61:237–269.

Guo, Z. J.; Shi, H. Y.; Zhang, Z. C.; and Zhang, J. J. 2006. The tectonic evolution of the south Tianshan paleo-oceanic crust inferred from the spreading structures and Ar-Ar dating of the Hongliuhe ophiolite, NW China. Acta Petrol. Sin. 22:95–102 (in Chinese with English abstract).

Han, B. F.; He, G. Q.; Wang, X. C.; and Guo, Z. J. 2011. Late Carboniferous collision between the Tarim and Kazakhstan-Yili terranes in the western segment of the South Tian Shan Orogen, Central Asia, and implications for the Northern Xinjiang, western China. Earth-Sci. Rev. 109:74–93.

Han, B. F.; Zhang, C.; Zhao, L.; Ren, R.; Xu, Z.; Chen, J. F.; Zhang, L.; Zhou, Y. Z.; and Song, B. 2010. A preliminary study of granitodis in western Inner Mongolia. Acta Petrol. Mineral. 29:741–749 (in Chinese with English abstract).

Han, Y. G.; Zhao, G. C.; Cawood, P. A.; Sun, M.; Eizenhöfer, P. R.; Hou, W. Z.; Zhang, X. R.; and Liu, Q. 2016*a*. Tarim and North China cratons linked to northern Gondwana through switching accretionary tectonics and collisional orogenesis. Geology 44:95–98.

Han, Y. G.; Zhao, G. C.; Sun, M.; Eizenhöfer, P. R.; Hou, W. Z.; Zhang, X. R.; Liu, Q.; Wang, B.; Liu, D. X.; and Xu, B. 2016*b*. Late Paleozoic subduction and collision processes during the amalgamation of the Central Asian Orogenic Belt along the South Tianshan suture zone. Lithos 246–247:1–12.

Hawkesworth, C. J., and Kemp, A. I. S. 2006. Using hafnium and oxygen isotopes in zircons to unravel the record of crustal evolution. Chem. Geol. 226:144–162.

He, Z. Y.; Sun, L. X.; Mao, L. J.; Zong, K. Q.; and Zhang, Z. M. 2015. Zircon U-Pb and Hf isotopic study of gneiss and granodiorite from the southern Beishan orogenic collage: Mesoproterozoic magmatism and crustal growth. Chin. Sci. Bull. 60(4):389–399 (in Chinese).

Irvine, T. N. J., and Baragar, W. 1971. A guide to the chemical classification of the common volcanic rocks. Can. J. Earth Sci. 8:523–548.

Jackson, S. E.; Pearson, N. J.; Griffin, W. L.; and Belousova, E. A. 2004. The application of laser ablation-inductively coupled plasma-mass spectrometry to in situ U-Pb zircon geochronology. Chem. Geol. 211:47–69.

Jiang, H. Y.; He, Z. Y.; Zong, K. Q.; Zhang, Z. M.; and Zhao, Z. D. 2013. Zircon U-Pb dating and Hf isotopic studies on the Beishan complex in the southern Beishan orogenic belt. Acta Petrol. Sin. 29:3949–3967 (in Chinese with English abstract).

Karsli, O.; Dokuz, A.; Uysal, İ.; Aydin, F.; Kandemir, R.; and Wijbrans, J. 2010. Generation of the early Cenozoic adakitic volcanism by partial melting of mafic lower crust, eastern Turkey: implications for crustal thickening to delamination. Lithos 114(1):109–120.

Kemp, A. I. S.; Hawkesworth, C. J.; Collins, W. J.; Gray, C. M.; Blevin, P. L.; and Edinburgh Ion Microprobe Facility. 2009. Isotopic evidence for rapid continental growth in an extensional accretionary orogen: the Tasmanides, eastern Australia. Earth Planet. Sci. Lett. 284:455–466.

Kemp, A. I. S.; Hawkesworth, C. J.; Paterson, B. A.; Foster, G. L.; Kinny, P. D.; Whitehouse, M. J.; Maas, R.; and Edinburgh Ion Microprobe Facility. 2008. Exploring the plutonic-volcanic link: a zircon U-Pb, Lu-Hf and O isotope study of paired volcanic and granitic units from southeastern Australia. Earth Environ. Sci. Trans. R. Soc. Edinb. 97:337–355.

Khain, E. V.; Bibikova, E. V.; Salnikova, E. B.; Kröner, A.; Gibsher, A. S.; Didenko, A. N.; Degtyarev, K. E.; and Fedotova, A. A. 2003. The Palaeo-Asian ocean in the Neoproterozoic and early Palaeozoic: new geochronologic data and palaeotectonic reconstructions. Precambrian Res. 122:329–358.

Klemd, R.; John, T.; Scherer, E. E.; Rondenay, S.; and Gao, J. 2011. Changes in dip of subducted slabs at depth: petrological and geochronological evidence from HP-UHP rocks (Tianshan, NW-China). Earth Planet. Sci. Lett. 310:9–20.

Li, S.; Wang, T.; Wilde, S. A.; Tong, Y.; Hong, D. W.; and Guo, Q. Q. 2012. Geochronology, petrogenesis and tectonic implications of Triassic granitoids from Beishan, NW China. Lithos 134:123–145.

Liu, C.; Zhao, Z. H.; and Guo, Z. J. 2006. Chronology and geochemistry of lamprophyre dykes from Beishan area, Gansu Province and implications for the crust-mantle interaction. Acta Petrol. Sin. 22:1294–1306 (in Chinese with English abstract).

Liu, Q.; Zhao, G. C.; Han, Y. G.; Eizenhöfer, P. R.; Zhu, Y. L.; Hou, W. Z.; Zhang, X. R.; and Wang, B. 2017*a*. Geochronology and geochemistry of Permian to Early Triassic granitoids in the Alxa Terrane: constraints on

the final closure of the Paleo-Asian Ocean. Lithosphere 9:665–680.

———. 2017*b*. Timing of the final closure of the Paleo-Asian Ocean in the Alxa Terrane: constraints from geochronology and geochemistry of Late Carboniferous to Permian gabbros and diorites. Lithos 274–275:19–30.

Liu, Q.; Zhao, G. C.; Sun, M.; Eizenhöfer, P. R.; Han, Y. G.; Hou, W. Z.; Zhang, X. R.; Wang, B.; Liu, D. X.; and Xu, B. 2015. Ages and tectonic implications of Neoproterozoic ortho- and paragneisses in the Beishan Orogenic Belt, China. Precambrian Res. 266:551–578.

Liu, Q.; Zhao, G. C.; Sun, M.; Han, Y. G.; Eizenhöfer, P. R.; Hou, W. Z.; Zhang, X. R.; et al. 2016. Early Paleozoic subduction processes of the Paleo-Asian Ocean: insights from geochronology and geochemistry of Paleozoic plutons in the Alxa Terrane. Lithos 262:546–560.

Liu, Y. S.; Hu, Z. C.; Zong, K. Q.; Gao, C. G.; Gao, S.; Xu, J.; and Chen, H. H. 2010. Reappraisement and refinement of zircon U-Pb isotope and trace element analyses by LA-ICP-MS. Chin. Sci. Bull. 55:1535–1546.

Long, X. P.; Yuan, C.; Sun, M.; Xiao, W. J.; Zhao, G. C.; Zhou, K. F.; Wang, Y. J.; and Hu, A. Q. 2011. The discovery of the oldest rocks in the Kuluketage area and its geological implications. Sci. China Ser. D Earth Sci. 54:342–348.

Long, X. P.; Yuan, C.; Sun, M.; Zhao, G. C.; Xiao, W. J.; Wang, Y. J.; Yang, Y. H.; and Hu, A. Q. 2010. Archean crustal evolution of the northern Tarim craton, NW China: zircon U-Pb and Hf isotopic constraints. Precambrian Res. 180:272–284.

Ludwig, K. R. 2003. User's manual for Isoplot 3.00: a geochronological toolkit for Microsoft Excel. Spec. Publ. 4. Berkeley, CA, Berkeley Geochronology Centre.

Maniar, P. D., and Piccoli, P. M. 1989. Tectonic discrimination of granitoids. Geol. Soc. Am. Bull. 101:635–643.

Mao, Q. G.; Xiao, W. J.; Windley, B. F.; Han, B. F.; Han, C. M.; Qu, J. F.; Ao, S. J.; Zhang, J. E.; and Guo, Q. Q. 2012. The Liuyuan complex in the Beishan, NW China: a Carboniferous–Permian ophiolitic fore-arc sliver in the southern Altaids. Geol. Mag. 149:483–506.

Martin, H.; Smithies, R. H.; Rapp, R.; Moyen, J.-F.; and Champion, D. 2005. An overview of adakite, tonalite-trondhjemite-granodiorite (TTG), and sanukitoid: relationships and some implications for crustal evolution. Lithos 79:1–24.

McDonough, W. F., and Sun, S. S. 1995. The composition of the Earth. Chem. Geol. 120:223–253.

Middlemost, E. A. K. 1994. Naming materials in the magma/igneous rock system. Earth-Sci. Rev. 37:215–224.

Miller, J. S.; Matzel, J. E. P.; Miller, C. F.; Burgess, S. D.; and Miller, R. B. 2007. Zircon growth and recycling during the assembly of large, composite arc plutons. J. Volcanol. Geotherm. Res. 167(1):282–299.

Miller, S. A.; van der Zee, W.; Olgaard, D. L.; and Connolly, J. A. D. 2003. A fluid-pressure feedback model of dehydration reactions: experiments, modelling, and application to subduction zones. Tectonophysics 370:241–251.

Patiño Douce, A. E. P. 1999. What do experiments tell us about the relative contributions of crust and mantle to the origin of granitic magmas? *In* Castro, A.; Fernández, C.; and Vigneresse, J. L., eds. Understanding granites: integrating new and classical techniques. Geol. Soc. Lond. Spec. Publ. 168:55–75.

Pearce, J. A. 1996. Sources and settings of granitic rocks. Episodes 19:120–125.

Pearce, J. A.; Harris, N. B. W.; and Tindle, A. G. 1984. Trace element discrimination diagrams for the tectonic interpretation of granitic rocks. J. Petrol. 25:956–983.

Peccerillo, A., and Taylor, S. R. 1976. Geochemistry of Eocene calc-alkaline volcanic rocks from the Kastamonu area, northern Turkey. Contrib. Mineral. Petrol. 58:63–81.

Pitcher, W. 1983. Granite types and tectonic environment. *In* Hsü, K., ed. Mountain building processes. London, Academic Press, p. 19–40.

Potts, P. J.; Thompson, M.; Kane, J. S.; and Petrov, L. L. 2000. GeoPT7—an international proficiency test for analytical geochemistry laboratories—report on round 7 (GBPG-1 garnet-biotite plagiogneiss). http://www.geoanalyst.org/wp-content/uploads/2017/10/GeoPT07Report.pdf.

Potts, P. J.; Thompson, M.; Webb, P. C.; and Watson, J. S. 2001. GeoPT9. An international proficiency test for analytical geochemistry laboratories—report on round 9/July 2001 (OU-6 Penrhyn slate). http://www.geoanalyst.org/wp-content/uploads/2017/10/GeoPT09Report.pdf.

Qi, L.; Hu, J.; and Grégoire, D. C. 2000. Determination of trace elements in granites by inductively coupled plasma mass spectrometry. Talanta 51:507–513.

Reubi, O., and Blundy, J. 2009. A dearth of intermediate melts at subduction zone volcanoes and the petrogenesis of arc andesites. Nature 461:1269–1273.

Roberts, N. M. W.; Slagstad, T.; Parrish, R. R.; Norry, M. J.; Marker, M.; and Horstwood, M. S. A. 2013. Sedimentary recycling in arc magmas: geochemical and U-Pb-Hf-O constraints on the Mesoproterozoic Suldal Arc, SW Norway. Contrib. Mineral. Petrol. 165:507–523.

Royden, L., and Burchfiel, B. C. 1989. Are systematic variations in thrust belt style related to plate boundary processes? (the western Alps versus the Carpathians). Tectonics 8:51–61.

Scherer, E.; Münker, C.; and Mezger, K. 2001. Calibration of the lutetium-hafnium clock. Science 293:683–687.

Şengör, A. M. C.; Natal'in, B. A.; and Burtman, V. S. 1993. Evolution of the Altaid tectonic collage and Palaeozoic crustal growth in Eurasia. Nature 364:299–307.

Shi, X. J.; Wang, T.; Zhang, L.; Castro, A.; Xiao, X. C.; Tong, Y.; Zhang, J. J.; Guo, L.; and Yang, Q. D. 2014*a*. Timing, petrogenesis and tectonic setting of the late Paleozoic gabbro-granodiorite-granite intrusions in the Shalazhashan of northern Alxa: constraints on the southernmost boundary of the Central Asian Orogenic Belt. Lithos 208–209:158–177.

Shi, X. J.; Zhang, L.; Wang, T.; Xiao, X. C.; Tong, Y.; Zhang, J. J.; Geng, J. Z.; and Ye, K. 2014*b*. Geochronology and geochemistry of the intermediate-acid intrusive rocks from Zongnaishan area in northern Alxa, Inner Mon-

golia, and their tectonic implications. Acta Petrol. Mineral. 33:989–1007 (in Chinese with English abstract).

Smits, R. G.; Collins, W. J.; Hand, M.; Dutch, R.; and Rayne, J. 2014. A Proterozoic Wilson cycle identified by Hf isotopes in central Australia: implications for the assembly of Proterozoic Australia and Rodinia. Geology 42:231–234.

Soesoo, A.; Bons, P. D.; Gray, D. R.; and Foster, D. A. 1997. Divergent double subduction: tectonic and petrologic consequences. Geology 25(8):755–758.

Song, D. F.; Xiao, W. J.; Han, C. M.; Tian, Z. H.; and Wang, Z. M. 2013. Provenance of metasedimentary rocks from the Beishan orogenic collage, southern Altaids: constraints from detrital zircon U-Pb and Hf isotopic data. Gondwana Res. 24:1127–1151.

Sylvester, P. J. 1998. Post-collisional strongly peraluminous granites. Lithos 45:29–44.

Tepley, F. J.; Davidson, J. P.; Tilling, R. I.; and Arth, J. G. 2000. Magma mixing, recharge and eruption histories recorded in plagioclase phenocrysts from El Chichon volcano, Mexico. J. Petrol. 41:1397–1411.

Thompson, M.; Potts, P. J.; Kane, J. S.; and Wilson, S. 2000. GeoPT5. An international proficiency test for analytical geochemistry laboratories—report on round 5 (August 1999). Geostand. Newsl. 24:E1–E28.

Tian, Z. H.; Xiao, W. J.; Shan, Y. H.; Windley, B. F.; Han, C. M.; Zhang, J. E.; and Song, D. F. 2013. Mega-fold interference patterns in the Beishan orogen (NW China) created by change in plate configuration during Permo-Triassic termination of the Altaids. J. Struct. Geol. 52:119–135.

Vervoort, J. D., and Blichert-Toft, J. 1999. Evolution of the depleted mantle: Hf isotope evidence from juvenile rocks through time. Geochim. Cosmochim. Acta 63: 533–556.

Wang, B.; Shu, L. S.; Faure, M.; Jahn, B. M.; Cluzel, D.; Charvet, J.; Chung, S. L.; and Meffre, S. 2011. Paleozoic tectonics of the southern Chinese Tianshan: insights from structural, chronological and geochemical studies of the Heiyingshan ophiolitic mélange (NW China). Tectonophysics 497:85–104.

Wang, T.; Zheng, Y. D.; Gehrels, G. E.; and Mu, Z. G. 2001. Chronology evidence of south Mongolia existed: zircon U-Pb ages of the Yagan-Wengqihaierhan core complex granitic gneiss. Chin. Sci. Bull. 46:1220–1223 (in Chinese with English abstract).

Wang, T.; Zheng, Y. D.; Li, T. B.; and Gao, Y. J. 2004. Mesozoic granitic magmatism in extensional tectonics near the Mongolian border in China and its implications for crustal growth. J. Asian Earth Sci. 23(5):715–729.

Wang, T. Y.; Wang, S. Z.; and Wang, J. R. 1994. The formation and evolution of Paleozoic continental crust in Alxa Region. Lanzhou, Lanzhou University Press, 213 p. (in Chinese).

Wang, Y.; Luo, Z. H.; Santosh, M.; Wang, S. Z.; and Wang, N. 2017. The Liuyuan Volcanic Belt in NW China revisited: evidence for Permian rifting associated with the assembly of continental blocks in the Central Asian Orogenic Belt. Geol. Mag. 154(2):265–285.

Wang, Z. Z.; Han, B. F.; Feng, L. X.; and Liu, B. 2015. Geochronology, geochemistry and origins of the Paleozoic-Triassic plutons in the Langshan area, western Inner Mongolia, China. J. Asian Earth Sci. 97:337–351.

Whalen, J. B.; Currie, K. L.; and Chappell, B. W. 1987. A-type granites: geochemical characteristics, discrimination and petrogenesis. Contrib. Mineral. Petrol. 95: 407–419.

Whitehouse, M. J.; Kamber, B. S.; and Moorbath, S. 1999. Age significance of U-Th-Pb zircon data from early Archaean rocks of West Greenland—a reassessment based on combined ion-microprobe and imaging studies. Chem. Geol. 160(3):201–224.

Wiedenbeck, M.; Allé, P.; Corfu, F.; Griffin, W. L.; Meier, M.; Oberli, F.; von Quadt, A.; Roddick, J. C.; and Spiegel, W. 1995. Three natural zircon standards for U-Th-Pb, Lu-Hf, trace element and REE analyses. Geostand. Newsl. 19:1–23.

Wilhem, C.; Windley, B. F.; and Stampfli, G. M. 2012. The Altaids of Central Asia: a tectonic and evolutionary innovative review. Earth-Sci. Rev. 113:303–341.

Windley, B. F.; Alexeiev, D.; Xiao, W. J.; Kröner, A.; and Badarch, G. 2007. Tectonic models for accretion of the Central Asian Orogenic Belt. J. Geol. Soc. Lond. 164:31–47.

Wu, T. R.; He, G. Q.; and Zhang, C. 1998. On Paleozoic tectonics in the Alxa region. Acta Geol. Sin. 72:256–263 (in Chinese with English abstract).

Xiao, W. J.; Mao, Q. G.; Windley, B. F.; Han, C. M.; Qu, J. F.; Zhang, J. E.; Ao, S. J.; et al. 2010. Paleozoic multiple accretionary and collisional processes of the Beishan orogenic collage. Am. J. Sci. 310:1553–1594.

Xiao, W. J.; Windley, B. F.; Allen, M. B.; and Han, C. M. 2013. Paleozoic multiple accretionary and collisional tectonics of the Chinese Tianshan orogenic collage. Gondwana Res. 23:1316–1341.

Xiao, W. J.; Windley, B. F.; Huang, B. C.; Han, C. M.; Yuan, C.; Chen, H. L.; Sun, M.; Sun, S.; and Li, J. L. 2009. End-Permian to mid-Triassic termination of the accretionary processes of the southern Altaids: implications for the geodynamic evolution, Phanerozoic continental growth, and metallogeny of Central Asia. Int. J. Earth Sci. 98: 1189–1217.

Xiao, W. J.; Windley, B. F.; Sun, S.; Li, J. L.; Huang, B. C.; Han, C. M.; Yuan, C.; Sun, M.; and Chen, H. L. 2015. A tale of amalgamation of three Permo-Triassic collage systems in central Asia: oroclines, sutures, and terminal accretion. Annu. Rev. Earth Planet. Sci. 43:477–507.

Xiong, F. H.; Ma, C. Q.; Zhang, J. Y.; and Liu, B. 2012. The origin of mafic microgranular enclaves and their host granodiorites from East Kunlun, northern Qinghai-Tibet Plateau: implications for magma mixing during subduction of Paleo-Tethyan lithosphere. Mineral. Petrol. 104(3–4):211–224.

Xu, B.; Charvet, J.; Chen, Y.; Zhao, P.; and Shi, G. Z. 2013. Middle Paleozoic convergent orogenic belts in western Inner Mongolia (China): framework, kinematics, geochronology and implications for tectonic evolution of the Central Asian Orogenic Belt. Gondwana Res. 23:1342–1364.

Ye, X. F.; Zong, K. Q.; Zhang, Z. M.; He, Z. Y.; Liu, Y. S.; Hu, Z. C.; and Wang, W. 2013. Geochemistry of Neoproterozoic granite in Liuyuan area of southern Beishan orogenic belt and its geological significance. Geol. Bull. China 32:307–317 (in Chinese with English abstract).

Yu, F. S.; Li, J. B.; and Wang, T. 2006. The U-Pb isotopic age of zircon from Hongliuhe ophiolites in east Tianshan Mountains, Northwest China. Acta Geosci. Sin. 27:213–216 (in Chinese with English abstract).

Yu, J. H.; O'Reilly, S. Y.; Zhao, L.; Griffin, W. L.; Zhang, M.; Zhou, X.; Jiang, S. Y.; Wang, L. J.; and Wang, R. C. 2007. Origin and evolution of topaz-bearing granites from the Nanling Range, South China: a geochemical and Sr-Nd-Hf isotopic study. Mineral. Petrol. 90(3):271–300.

Yu, J. H.; Zhou, X. M.; Zhao, L.; Jiang, S. Y.; Wang, L. J.; and Ling, H. F. 2005. Mantle-crust interaction generating the Wuping granites: evidenced from Sr-Nd-Hf-U-Pb isotopes. Acta Petrol. Sin. 21:651–664 (in Chinese with English abstract).

Zhang, J. X.; Gong, J. H.; Yu, S. Y.; Li, H. K.; and Hou, K. J. 2013. Neoarchean–Paleoproterozoic multiple tectonothermal events in the western Alxa block, North China Craton and their geological implication: evidence from zircon U-Pb ages and Hf isotopic composition. Precambrian Res. 235:36–57.

Zhang, S. H.; Zhao, Y.; Liu, J. M.; Hu, J. M.; Song, B.; Liu, J.; and Wu, H. 2010. Geochronology, geochemistry and tectonic setting of the late Paleozoic-early Mesozoic magmatism in the northern margin of the North China Block: a preliminary review. Acta Petrol. Mineral. 29:824–842 (in Chinese with English abstract).

Zhang, X. R.; Zhao, G. C.; Eizenhöfer, P. R.; Sun, M.; Han, Y. G.; Hou, W. Z.; Liu, D. X.; Wang, B.; Liu, Q.; and Xu, B. 2015*a*. Latest Carboniferous closure of the Junggar Ocean constrained by geochemical and zircon U-Pb-Hf isotopic data of granitic gneisses from the Central Tianshan block, NW China. Lithos 238:26–36.

———. 2015*b*. Paleozoic magmatism and metamorphism in the Central Tianshan block revealed by U-Pb and Lu-Hf isotope studies of detrital zircons from the South Tianshan belt, NW China. Lithos 233:193–208.

———. 2016. Tectonic evolution from subduction to arc-continent collision of the Junggar ocean: constraints from U-Pb dating and Hf isotopes of detrital zircons from the North Tianshan belt, NW China. Geol. Soc. Am. Bull. 128:644–660.

Zhang, Y. Y.; Dostal, J.; Zhao, Z. H.; Liu, C.; and Guo, Z. J. 2011. Geochronology, geochemistry and petrogenesis of mafic and ultramafic rocks from southern Beishan area, NW China: implications for crust-mantle interaction. Gondwana Res. 20:816–830.

Zhang, Y. Y., and Guo, Z. J. 2008. Accurate constraint on formation and emplacement age of Hongliuhe ophiolite, boundary region between Xinjiang and Gansu Provinces and its tectonic implications. Acta Petrol. Sin. 24:803–809 (in Chinese with English abstract).

Zhao, G. C.; Sun, M.; Wilde, S. A.; and Li, S. Z. 2005. Late Archean to Paleoproterozoic evolution of the North China Craton: key issues revisited. Precambrian Res. 136:177–202.

Zhao, G. C.; Wilde, S. A.; Cawood, P. A.; and Sun, M. 2001. Archean blocks and their boundaries in the North China Craton: lithological, geochemical, structural and *P-T* path constraints and tectonic evolution. Precambrian Res. 107:45–73.

Zheng, R. G.; Wu, T. R.; Zhang, W.; Feng, J. C.; Xu, C.; Meng, Q.; and Zhang, Z. Y. 2013. Geochronology and geochemistry of the Yagan granite in the northern margin of the Alxa block: constraints on the tectonic evolution of the southern Altaids. Acta Petrol. Sin. 29:2665–2675 (in Chinese with English abstract).

Zheng, R. G.; Wu, T. R.; Zhang, W.; Xu, C.; Meng, Q. P.; and Zhang, Z. Y. 2014. Late Paleozoic subduction system in the northern margin of the Alxa block, Altaids: geochronological and geochemical evidences from ophiolites. Gondwana Res. 25:842–858.

Zheng, Y. F.; Chen, Y. X.; Dai, L. Q.; and Zhao, Z. F. 2015. Developing plate tectonics theory from oceanic subduction zones to collisional orogens. Sci. China Ser. D Earth Sci. 585:1045–1069.

Zheng, Y. F.; Zhang, S. B.; Zhao, Z. F.; Wu, Y. B.; Li, X. H.; Li, Z. X.; and Wu, F. Y. 2007. Contrasting zircon Hf and O isotopes in the two episodes of Neoproterozoic granitoids in South China: implications for growth and reworking of continental crust. Lithos 96:127–150.

Zhou, X. M., and Li, W. X. 2000. Origin of late Mesozoic igneous rocks in southeastern China: implications for lithosphere subduction and underplating of mafic magmas. Tectonophysics 326(3):269–287.